Human Molecular Genetics, 2011 ***1–23***
doi:10.1093/hmg/ddr494

Loss of ceramide synthase 3 causes lethal skin barrier disruption

Richard Jennemann[1,†], Mariona Rabionet[1,2,†], Karin Gorgas[4], Sharon Epstein[7], Alexander Dalpke[5], Ulrike Rothermel[1], Aline Bayerle[1,2], Franciscus van der Hoeven[3], Silke Imgrund[8], Joachim Kirsch[4], Walter Nickel[6], Klaus Willecke[8], Howard Riezman[7], Hermann-Josef Gröne[1] and Roger Sandhoff[1,2,9,*]

[1]Cellular & Molecular Pathology, [2]Lipid Pathobiochemistry Group, INF 280 and [3]Transgen-Service, German Cancer Research Center, 69120 Heidelberg, Germany, [4]Institute of Anatomy and Cell Biology, [5]Medical Microbiology and Hygiene and [6]Biochemistry Center, Universtity of Heidelberg, 69120 Heidelberg, Germany, [7]Department of Biochemistry, University of Geneva, CH-1211 Geneva, Switzerland, [8]LIMES Institute, Genetics, University of Bonn, 53115 Bonn, Germany and [9]Instrumental Analytics and Bioanalytics, Mannheim University of Applied Sciences, 68163 Mannheim, Germany

Received August 18, 2011; Revised and Accepted October 23, 2011

The stratum corneum as the outermost epidermal layer protects against exsiccation and infection. Both the underlying cornified envelope (CE) and the intercellular lipid matrix contribute essentially to these two main protective barriers. Epidermis-unique ceramides with ultra-long-chain acyl moities (ULC-Cers) are key components of extracellular lipid lamellae (ELL) and are bound to CE proteins, thereby contributing to the cornified lipid envelope (CLE). Here, we identified human and mouse ceramide synthase 3 (CerS3), among CerS1–6, to be exclusively required for the ULC-Cer synthesis *in vitro* and of mouse CerS3 *in vivo*. Deficiency of CerS3 in mice results in complete loss of ULC-Cers (≥C26), lack of continuous ELL and a non-functional CLE. Consequently, newborn mutant mice die shortly after birth from transepidermal water loss. Mutant skin is prone to *Candida albicans* infection highlighting ULC-Cers to be pivotal for both barrier functions. Persistent periderm, hyperkeratosis and deficient cornification are hallmarks of mutant skin demonstrating loss of Cers to trigger a keratinocyte maturation arrest at an embryonic pre-barrier stage.

INTRODUCTION

The multilayered epidermis of mammalian skin represents the first protective barrier towards environment. When the two main barrier functions against transepidermal water loss (TEWL) and pathogen invasion become deficient, such as in ichthyosis, atopic dermatitis and psoriasis, specific, indispensable barrier components of the cornified epidermal layer, particularly the cornified envelope (CE) and the extracellular lipid lamellae (ELL), are severely altered. Intracellularly, lipid precursors of the ELL are packed into membrane-limited, tubulovesicular lamellar bodies (LBs) during keratinocyte maturation together with a variety of proteins, including hydrolytic enzymes and antimicrobial peptides. LBs are preferentially extruded at the interface between the viable and anuclear epidermal layers, i.e. the stratum granulosum (SG) and the stratum corneum (SC), respectively. A key regulator of this secretory process is an extracellular calcium gradient (1,2).

Alignment of LB content into mature ELL requires sequential extracellular processing of lipid precursors, glucosylceramides (GlcCers) and phospholipids, and establishment of the cornified lipid envelope (CLE), a lipid monolayer covalently bound to the CE and crucial for the competence of the water permeability barrier (WPB). ELL contain high levels of Cers with ultra-long-chain (ULC) (C28–C36) omega-hydroxylated acyl moieties (abbreviated here as ωh-Cers) (1), which are to a

*To whom correspondence should be addressed at: DKFZ-G131, INF 280, 69120 Heidelberg, Germany. Tel: +49 6221424358; Fax: +49 6221424352; Email: r.sandhoff@dkfz.de
†These authors contributed equally to this work and are listed in alphabetical order.

great extent ω-esterified either to fatty acids (FAs), predominantly linoleic acid or to carboxylic acid moities of cross-linked CE proteins forming the CLE. During terminal cornification, ωh-Cers are degraded to yield the corresponding FAs and sphingosine (3). Importantly, the latter has been shown to have anti-microbial activity *in vitro* (4–7). Details of ωh-Cer biosynthesis and their intracellular transport as well as the biogenesis and secretion of LBs are incompletely understood at a molecular level. However, definite knowledge of these processes and their regulation is of fundamental importance for understanding skin pathophysiology, a prerequisite for targeted therapy.

The biodiversity of Cer species arising in human SC from 12 subclasses (8) requires a family of genes, the *CERS* family (*Cers1–6* in mammals) (9). Depending on the substrate specifity towards the length of the acyl-CoAs and the degree of saturation, each of these enzymes synthesizes a subset of Cer species. Whereas CerS have been identified for the incorporation of long-chain (LC, C16–20) and very long-chain (VLC, C22–26) acyl moieties (10), a distinct member for ULC-acyl CoA substrates (>C26) remains elusive.

The prominent coexpression of CerS3 and of ULC-sphingolipids (ULC-SLs) in skin and testis suggested CerS3 in the biosynthesis of ωh-Cers in the epidermis (11–13). Here, we show by expressing CerS3 in yeast and human cell cultures and by analyzing the epidermal lipids of CerS2- and CerS3-deficient mice that CerS3 function cannot be replaced by one of the other five CerS. Evidence is provided that CerS3-deficient mice lack all SLs with ULC-FAs resulting in WPB disruption, and that mutant skin enables pathogen invasion (*Candida albicans*). We demonstrate absence of ωh-Cers to trigger an epidermal maturation arrest at an embryonic pre-barrier stage. Hallmarks of CerS3 mutant mouse skin include discontinuity of ELL, impairment of CLE as shown with unmasked loricrin, hyperkeratosis, persistence of periderm and non-peripheral corneodesmosomes (CDs) and defective profilaggrin processing. Our data demonstrate ULC-Cers to be engaged in cornification and apoptosis of peridermal cells.

RESULTS

Ultra-long-chain FAs are bona fide substrates of CerS3

From CerS1–6, only CerS2 and CerS3 accept VLC acyl-CoAs (C22–C26) for the (dihydro-)Cer synthesis (11). To prove our hypothesis CerS3 to be needed for ULC-Cer production, a non-radioactive and detergent-free enzymatic assay with a range of FAs including ULC-FA montanic acid (28:0), were performed in living HeLa cells and yeast expressing CerS2 or CerS3. In HeLa cells, mCerS3-enhanced green fluorescent protein (EGFP) localized to the endoplasmic reticulum (ER), but not to the Golgi or lysosomes (Fig. 1A_{1-3}). This expression is in line with the described acylation of sphingoid bases at the ER (10).

Endogenously, HeLa cells express all *Cers* mRNAs except for *Cers3* mRNA. The major transcripts were those of *Cers2*, consistent with the main Cer species containing C24:0. HeLa cells exposed to an acyl-CoA mixture (16–28:0-CoA) strongly synthesized Cers with cerotoyl (26:0) and montanoyl CoA (28:0) (~25% of total Cers) only upon induction of the transfected human and murine CerS3. The absolute cerotoyl-Cer amount was increased by 6-fold, while montanoyl Cer was increased at least 16-fold in case of hCerS3. With shorter acyl-CoAs, no increased incorporation was observed in the presence of CerS3. Cells overexpressing CerS2 or EGFP did not generate significant amounts of ULC-Cers (Fig. 1B–E).

The preference of CerS3 and the inability of CerS2 to accept ULC-acyl donors were confirmed in *Saccharomyces cerevisiae* synthesizing montanoyl CoA upon transformation with a mutant elongase protein (Sur4p*) (14). The Cer-anchor pattern of the downstream product inositolphosphorylceramide (IPC) was analysed in strains in which the yeast homologues, *LAG1* and *LAC1*, were exchanged for CerS2 or CerS3 under control of a yeast promoter. Montanoyl CoA was incorporated into IPC in the CerS3 strain, but not in the CerS2 strain confirming that montanoyl CoA is a *bona fide* substrate of CerS3. In addition, CerS3 accepted stearyl CoA (C18:0), lignoceroyl CoA (C24:0) and cerotoyl CoA (26:0) (Fig. 1F and G).

CerS2 is not involved in ULC-ceramide synthesis *in vivo*

Although CerS2 was excluded for ULC-Cer synthesis *in vitro*, its mRNA level was high in murine skin (Supplementary Material, Fig. S1A). However, $CerS2^{gt/gt}$ mice show no obvious skin phenotype and similar levels of epidermal Cer species, not even for Cer containing a lignoceroyl residue (24:0), the preferred product of CerS2 (Supplementary Material, Fig. S1B–C). Our results point to an indispensable role of CerS3 and exclude CerS2 from VLC/ULC Cer synthesis in epidermis.

CerS3 deficiency in mice leads to WPB disruption and neonatal death

To gain insight into the function of CerS3 *in vivo*, we generated mice with a disrupted *Cers3* gene. Phenotypically, $CerS3^{d/d}$ mice were easily distinguished from $CerS3^{+/d}$ and $CerS3^{+/+}$ mice, as their skin appeared unwrinkled, erythematous and sticky (Fig. 2A). Milk in the stomach of newborns (Fig. 2B) was only observed in controls consistent with the observation that the mother rejected mutant siblings. They died

Figure 1. CerS3 is located at the ER and synthesizes ULC-Cers in HeLa cells and in yeast. (**A_{1-3}**) mCerS3-EGFP colocalizes with the ER marker (Pdi), but not with those for Golgi (Golga1) or lysosomes (Lamp1). Nuclei, 4′,6-diamidino-2-phenylindole (DAPI). (**B**) Relative *de novo* Cer (d17:1) levels according to the length of their FA moieties in cells either not expressing (−) or expressing (+) recombinant hCerS2 or hCerS3, or (**D**) mCerS3 or EGFP control. Lipids were isolated 20 h after incubation with a saturated acyl-CoA mixture (C16, 18, 24, 26, 28-acyl-CoA) and sphingosine (d17:1). (**C**) Corresponding absolute concentrations of C26:0-Cer and (**E**) C28:0-Cer. (**F**) Relative IPC levels of wild-type (WT), mCerS2 and hCerS3 expressing *S. cerevisiae* transformed with WT (Sur4p) or mutant FA elongase (Sur4p*), the latter capable of C28:0-CoA synthesis. (**G**) Relative C26:0- and C28:0-IPC levels from mCerS2 and hCerS3 expressing cells after transformation with Sur4p or Sur4p*.

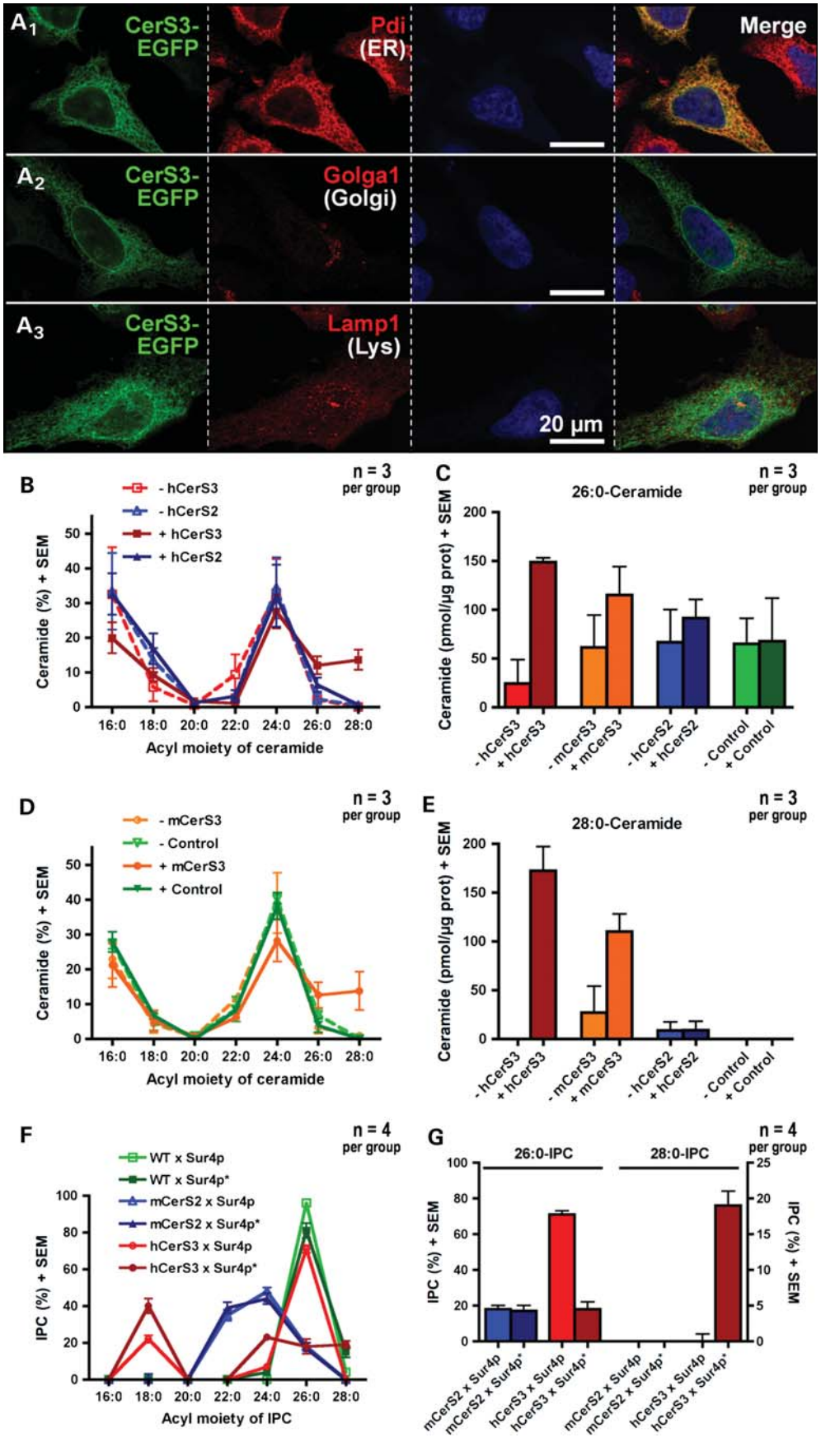

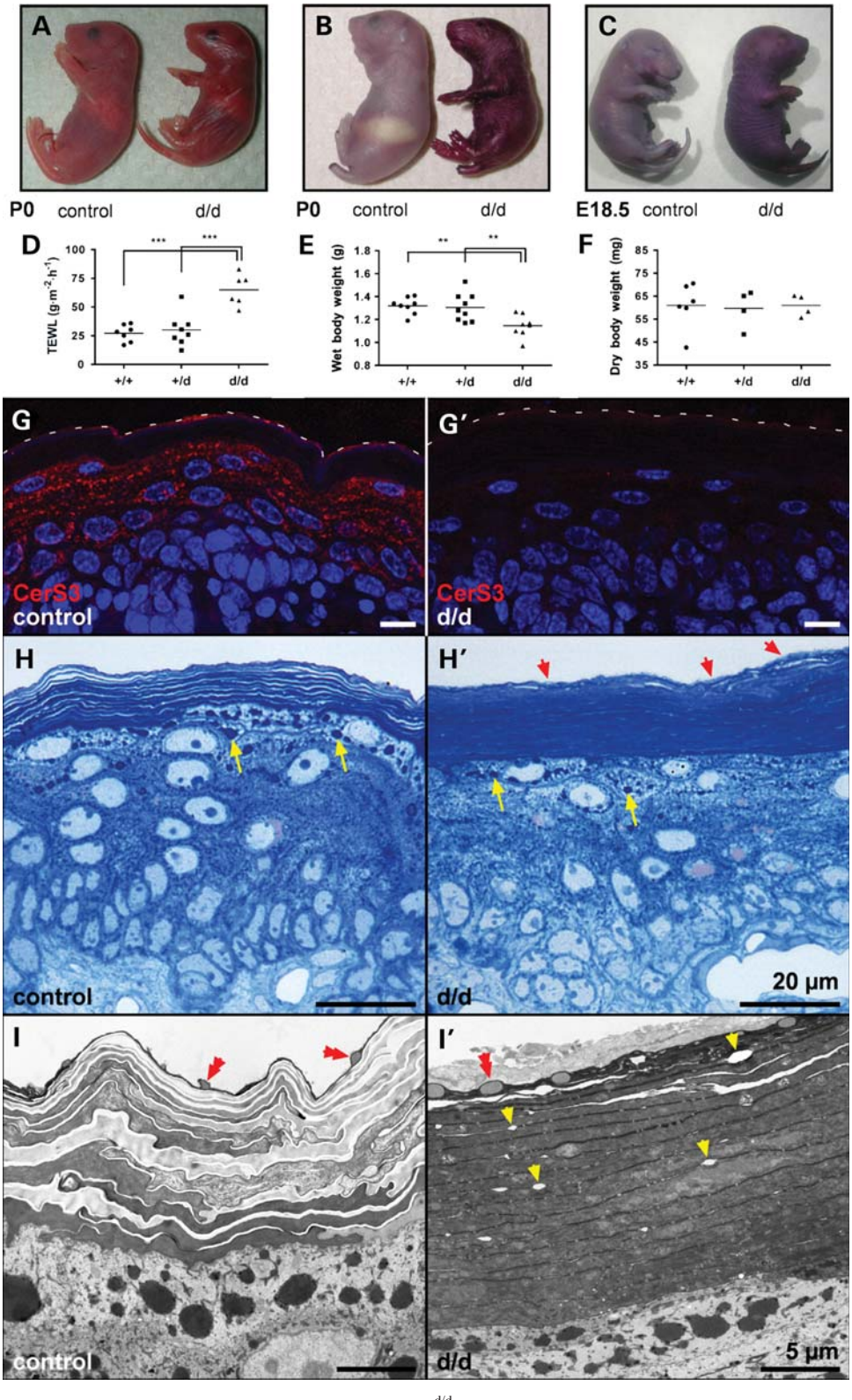

Figure 2. Defective epidermal barrier and absence of CerS3. (**A**) Neonatal CerS3$^{d/d}$ skin appears erythematous when compared with controls. (**B** and **C**) Mayer's hemalaun exclusion assay demonstrates defective epidermal barrier in both mutant newborns and embryos (E18.5 $\pm$ 0.5). (**D** and **E**) Significant increase in TEWL and reduced body wet weight in mutants are evident about 3 h after birth. (**F**) Dry body weights of mutant and control embryos (E18.5 $\pm$ 0.5) do not differ. (**G** and G′) Endogenous CerS3 appears clustered within upper SS and SG, whereas in mutants CerS3 is absent. Nuclei, DAPI. (**H** and H′) Semithin sections from neonatal control and mutant skin reveal thickened compact SC covered by a periderm (red arrows), and smaller KGs (yellow arrows) in mutants. PAS-methylene blue/azure II (**I** and I′) EM of the upper epidermal layers exhibit SC lipid lacunae (yellow arrowheads), absent stratum disjunctum and periderm on top of SC in mutants. The uppermost SC layer is marked by electron-lucent inclusion bodies in both controls and mutants (red double arrowheads). OsO_4/tannin.

within 3–4 h after birth and/or were devoured by the mother. It is reported that normal newborns which are not fed survive at least three times longer (12–24 h) than observed for CerS3 mutants excluding malnutrition as a cause for their neonatal death (15).

As the erythematous appearance suggested a compromised epidermal barrier, permeability assays were carried out. Mutants exhibited a strong dye penetration, indicating barrier impairment at birth and at embryonic stage (E18.5). The WPB is normally established between E17.5 and E18.5 (16) and indeed E18.5 controls were resistant to dye penetration (Fig. 2B and C). The permeability defect was corroborated by over 2-fold increased TEWL rates (Fig. 2D). As no differences in wet or dry body weight of E18.5 mutant and control embryos were found (Fig. 2F and Supplementary Material, Fig. S2F), the 30% decrease in body wet weight of newborn mutants (Fig. 2E) resulted obviously from desiccation. Keeping these data in mind, all studies were carried out in newborns directly after birth.

CerS3 localizes to upper stratum spinosum (SS) and SG

In order to confirm the loss of CerS3 in mutant skin at the protein level, we determined the epidermal localization of CerS3-dependent Cer synthesis. CerS3 clustered in scattered dots within keratinocytes of upper SS and SG. In contrast, CerS3 expression was not detected in mutants (Fig. 2G and G′), thereby indicating that deletion of exon 7 renders synthesis or stability of mutated CerS3 dysfunctional.

Epidermal maturation arrests at embryonic pre-barrier stage

To find out the cause of skin stickiness, mutant epidermal structure was analyzed after embedding skin in agar before sample processing. This approach provided an intact periderm on top of mutant SC. This protective embryonic cell layer, which is normally degraded in parallel to barrier formation, failed to shed in CerS3-depleted epidermis at E18.5 and P0 (Fig. 2H–I′, Supplementary Material, Figs S2I–J′ and S5A′).

Below the periderm, mutant SC was almost twice as thick with ∼40% more corneocyte layers constituting only a stratum compactum, but lacking a stratum disjunctum (Fig. 2H–I′ and Supplementary Material, Fig. S2I–J′). This hyperkeratosis appeared neither to result from altered desquamation or enhanced proliferation, as (i) corneocyte shedding had not taken place even in controls, as confirmed by the presence of the outermost corneocyte layer decorated with electron-lucent, F-actin-positive inclusion bodies (Figs 2I and I′ and 6B and B′), and (ii) the proliferation rate of basal keratinocytes was unchanged (Supplementary Material, Fig. S2M–N′) as proven by the distribution pattern of both Ki67 within interfollicular epidermis and cytokeratins Krt14 and Krt10 in the basal and suprabasal layers, respectively (Supplementary Material, Fig. S2K–L′). Hyperkeratosis was already obvious at E18.5 (Supplementary Material, Fig. S2J and J′), suggesting a failure in barrier formation to trigger mildly enhanced keratinocyte proliferation before birth.

Antimicrobial barrier is disturbed

Increased TEWL values and reduced epidermal Cer levels are, for example, described in patients with atopic dermatitis, highly susceptible for pathogen infection (4). Therefore, we tested whether the skin barrier of CerS3$^{d/d}$ mice was also prone to infections. As a model, we inoculated cultured skin samples of newborns with *C. albicans*, a common opportunistic pathogen colonizing the epidermis of patients with compromised skin integrity.

In contrast to controls, prominent pathogen adhesion to mutant SC was visible as early as 6 h after inoculation. As a result, focal proliferation of *C. albicans* and deep invasive infection into all epidermal layers was observed after 24 h (Fig. 3A–B′). At 66 h, increased colony formation occurred within lower epidermal layers, and additionally pseudohyphae that crossed the residual basement membrane migrated deep into the dermis which was marked by abundant immune cells (Fig. 3C′). This enhanced fungal attack was confirmed in E18.5 mutant embryos by the determination of the colony forming units (Supplementary Material, Fig. S2O).

Besides sphingosines, specific antimicrobial peptides are involved in cutaneous defense mechanisms against pathogens. These peptides are generally packed in LBs and extruded at the SG–SC interface (17,18). In mutant skin, a downregulation of antimicrobial peptide synthesis at the transcriptional level was not observed for β-defensins and cathelicidin (Supplementary Material, Fig. S2P), suggesting a direct inhibitory effect of sphingosine on *Candida* growth and invasion.

ULC ceramides are absent

We used thin layer chromatography (TLC) and quantitative mass spectrometry (MS) to evaluate the effects of CerS3 depletion on the epidermal lipid composition. TLC revealed that all Cer and GlcCer bands except the correspondingly lowest band were strongly reduced or absent in CerS3$^{d/d}$ mice. No significant differences could be observed between wild-type and heterozygous mice (Supplementary Material, Fig. S3A). MS further showed that all Cer, GlcCer and sphingomyelins with C26:0 or ULC-FA residues were lost. Since SLs with ULC-acyl moieties are the only sources of ωh-esterified SLs, all protein-bound Cers and all Cers ωh-esterified with linoleic acid were missing. Surprisingly, even SLs with lignoceroyl (24:0) residues were significantly diminished. Cer and GlcCer containing (hydroxylated) palmitate (16:0 or h16:0) residues were slightly elevated confirming TLC data. However, this increase did not compensate for the loss of ULC-SLs indicating CerS3$^{d/d}$ mice lack in total ∼90% of all epidermal Cers (Fig. 4C–F and Supplementary Material, Fig. S3B). Along with cornification, Cers are degraded to sphingosines and FAs. In line with lost Cers, we observed a decrease in sphingosines to ∼10% of control levels using a new MS assay (unpublished data).

Lipid barrier is disrupted, but corneocyte plasma membrane structure is conserved

GlcCers and phospholipids, including sphingomyelins, are precursors of Cers and free FAs. Together with cholesterol,

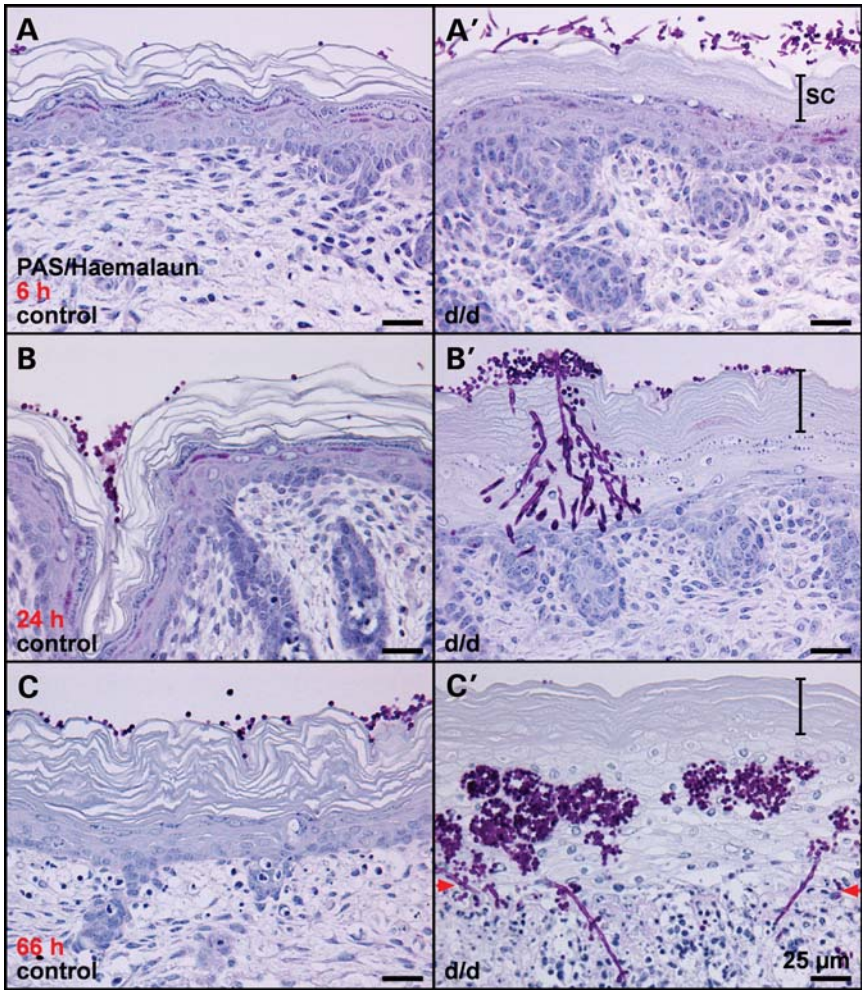

Figure 3. High skin susceptibility to Candida infection. (**A**–**C**′) Cultured skin samples of CerS3$^{d/d}$ mice reveal after inoculation with *C. albicans* increased microbial adhesion and growth after 6 h (A′), microbial invasion of all epidermal layers after 24 h (B′) and microbial colony formation within SS in parallel to migration of pseudohyphae into the dermis after 66 h (C′, the residual basement membrane, red arrowheads). Note the abundance of immune cells in mutant dermis after 66 h. PAS-hemalaun.

they are major ELL constituents. Present in an almost equimolar ratio, they are considered crucial for ELL organization and barrier competence. To assess the relevance of ULC-Cers for alignment of continuous ELL and establishment of CLE, we analyzed cholesterol (filipin) as well as neutral and polar lipid (Nile red) localization in correlation to the epidermal fine structure. Filipin and Nile red decorated corneocytes with uniform linear lipid structures throughout SC (Fig. 4A and B). In mutants, however, an abnormal, pearl-like lipid distribution was obvious (Fig. 4A′ and B′). The ultrastructural analysis confirmed the loss of lamellar structures within the upper SC. Minor amounts of secreted lipid clustered into small lentil-like lacunae (Figs 2I′ and 4H′–G′, and Supplementary Material, Fig. S5A′) often located at tricellular

Figure 4. Impaired SC lipid organization and epidermal lipid composition. (**A** and **B**′) Both cholesterol labeling with filipin (A and A′) and staining of polar and neutral lipids with Nile red (B and B′) reveal continuous linear lipid structures in control SC (A and B) which are replaced by a dot-like pattern in mutants (A′ and B′, white arrows). (**C**–**F**) MS quantification of epidermal Cers (C and F), GlcCers (D) and sphingomyelins (E, SM) of CerS3$^{+/+}$, CerS$^{+/d}$ and CerS$^{d/d}$ mice indicates loss of all SLs with acyl moieties longer than 24 C-atoms in mutants, including all SLs bound to linoleic acid or proteins. Cers with C24-acyl moieties are also significantly reduced (F). Non-esterified SLs (free) with acyl moieties smaller than 28 C-atoms (FA ≤ C26) or longer than 26 C-atoms (FA ≥ C28); EOS, SLs esterified to linoleic acid; POS, protein-bound SLs. (**G**′, **H**–**J**′) EM of SG and SC. (G′) Mutant upper SC interstices show highly approximated, ELL-free domains (yellow arrows) between adjacent corneocytes alternating with non-peripheral CDs (black arrows) or with focal, lentil-like lipid agglomerates (black asterisk) present from the second SC layer onwards (H′, red asterisks). (H and H′) SG–SC interface in controls exhibits abundant LB exocytosis marked by deep invaginations (red arrows), absent in mutants. Lamellar lipid-free domains exclusively occur in mutants (yellow arrows). (I–J′) Higher magnification reveals secreted lipid stacks in both controls and mutants. Mutant discs are rather shorter but arrange similar in parallel to the cell surface. (I′$_3$, inset) At high magnification, the trilaminar plasma membrane structure (b) of 8 nm thickness spaced by two electron-dense bands corresponding to the polar lipid head groups is clearly visible at the lamellar lipid-free interface (i). (G′–I′) OsO_4/tannin and (J–J′) RuO_4 postfixation. (J′) Red arrow, desmosome; red asterisk, lamellar discs at a tricellular contact site.

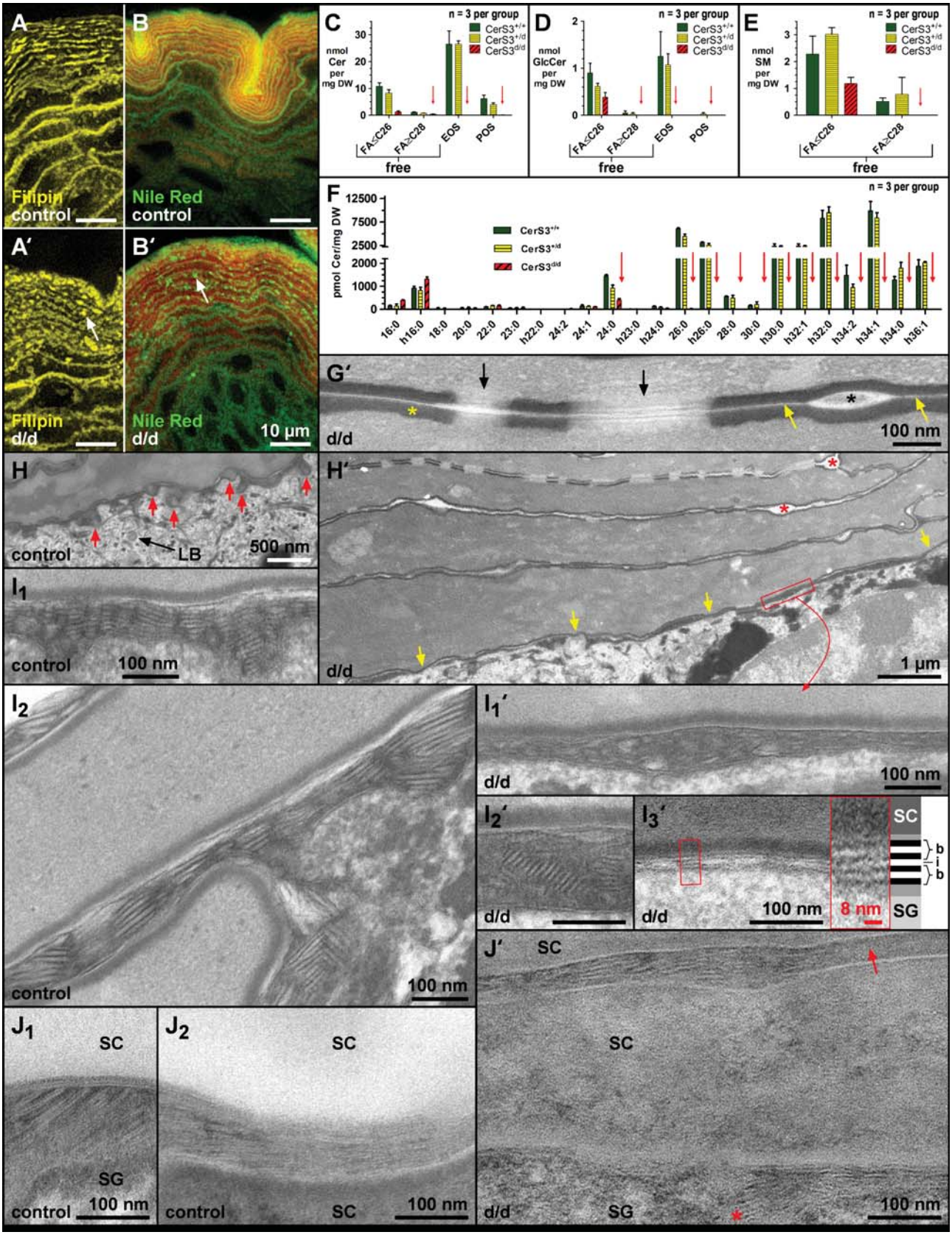

contact sites. Surprisingly, in the lower SC interstices and the interface, areas with ELL were observed in mutants (Fig. 4I_{1-3}' and J′). ELL appeared similar, independent of the postfixation method used (Fig. 4I_{1-2} and J_{1-2}, compare with mature LBs in Supplementary Material, Fig. S3C_{1-3}). These ELL alternated with ELL-free areas (Fig. 4H′ and I_3') suggesting insufficient lipid secretion by LBs at the mutant interface. Indeed, the latter appeared flattened, whereas in controls the interface was marked by deep invaginations filled with lamellar stacks reflecting abundant exocytosis (Fig. 4H and I_1). As a consequence, in mutant SC, the trilaminar plasma membrane structure of ∼8 nm in width persisted not only at the interface (Fig. 4I_3'), but also in the upper layers of SC (Fig. 4G′ and Supplementary Material, Fig. S5B′ and C′), including the outermost corneocyte layer (Fig. 6F_1'). Thus, the loss of ULC-Cers leads to impaired CLE and pore-like, ELL-free SC interstices responsible for enhanced TEWL.

Biogenesis and extrusion of LBs are accelerated

We next asked whether reduced secretion resulted from deficient intracellular LB formation. Besides lipids, lysosome-related LBs secrete lipases and proteases such as kallikrein 5 (Klk5) and cathepsin D (Ctsd) (19). Ctsd was used to trace LB distribution.

In controls, Ctsd labeled with high intensity the secretory front at the SG–SC interface and the sub-adjacent, uppermost SG layer. In mutants LB release, as monitored by Ctsd, was weak at the interface, but a new front located to the lower SG/SS as unequivocally confirmed by consecutive sections (Fig. 5A_{1-2} and A'_{1-2}). Concomitantly, Ctsd present in normal SC was lacking in mutant SC (Fig. 5A and A′), although prepro-Ctsd processing (unpublished data) and overall mature protein levels, similar to Klk5, were not altered (Fig. 7F). Fine structural analysis confirmed that in controls the greatest amount of LB exocytosis was found at the interface and unreleased LBs peaked at the apical surface of the second uppermost SG keratinocytes. In mutants, however, LB extrusion was limited at the interface and the highest number of unreleased LBs was detected within the third/fourth SG layer (Fig. 5D–E′), indicating both premature LB formation and accelerated LB release. The quantity of LBs seemed similar in mutants (Fig. 5E and E′), whereas the diameter of LBs was slightly decreased and enclosed lamellar stacks were often shortened and fragmented (Fig. 5E and E′, insets).

Abundant tubular–vesicular structures with similar dimensions as LBs were observed even within the uppermost SG, but were not altered ultrastructurally in mutants. To verify that these structures were not related to LBs, but represent peroxisomes, we tracked them using the peroxisomal membrane-anchored protein Pex14, a key component of the peroxisomal import machinery (20) and diaminobenzidine (DAB) for EM visualization of catalase. Abundance and shape of peroxisomes were confirmed by DAB (Fig. 5C_{TEM} for control). Pex14 staining revealed similar peroxisome density, but the peroxisome signal remarkably declined in mutant SG (Fig. 5C and C′). The proximity of LBs and peroxisomes in SG as well as a likely decreased peroxisomal import activity in mutants hints to a potential involvement of peroxisomes in ωh-Cer biosynthesis which remains to be clarified.

Non-peripheral CDs are preserved

A key question remained: how does CerS3 deficiency cause an arrest in SC maturation leading to cohesion of uppermost corneocytes and periderm? CDs as intercellular junctions are crucial in SC cohesion and proteases including Ctsd are required for their degradation (21). In the outer layers (stratum disjunctum), non-peripheral CDs are degraded leading to the typical ‘basket-weave’ appearance of control skin (Figs 2H and 3A–C). Both cohesion and degradation are controlled by pH, which decreases in the upper SC (22). Surprisingly, preliminary surface measurements on newborns showed a pH increase from 5.2 ± 0.1 to 5.8 ± 0.2 in mutants. As suggested, EM analysis revealed peripheral and non-peripheral CDs persisted in all mutant SC layers (Supplementary Material, Fig. S5A′), including the most superficial one (Fig. 6F'_{1-2}). Transformation of a desmosomal core into a homogeneous, electron-dense desmoglea was not observed (Supplementary Material, Fig. S5B–C′). In controls, non-peripheral CDs were restricted to stratum compactum and were lacking between uppermost SC layers (Fig. 6F). Correspondingly, desmoglein 1—a Ca^{2+}-dependent, cell bridging transmembrane cadherin and major component of suprabasal desmosomes and CDs—was preserved in mutant SC, including periderm visualizing thereby all CDs. In control SC, desmoglein 1 was not detected, even after alkaline treatment (Fig. 6A and A′) either due to masking or restricted degradation of the cytosolic desmoglein 1 domain, detected by the antibody. Nevertheless, the overall protein levels decreased in $CerS3^{d/d}$ epidermis (Fig. 7F). The desmosomal plaque proteins, desmoplakin 1/2 (Fig. 6E and E′) and plakoglobin (unpublished data), were not detectable in mutant and control SC implicating their degradation.

Peridermal cells, still containing nuclear remnants (Fig. 6D′) and occasionally cell organelles, were interconnected by desmosomes (Fig. 6F'_{3-4}) and to SC by CDs (Fig. 6F'_2). Additionally, TJs described for embryonic periderm (23) persisted between peridermal cells (Fig. 6C′ and F'_4). In controls, TJs were restricted to SS/SG, forming in the upper SG continuous linear structures (zonulae occludentes) which essentially contribute to the WPB (Fig. 6D) (24). Although no differences were observed for claudin-1 (Figs 6C and C′ and 7F), slightly thickened and curled strands were observed in mutant SG when labeled with cingulin, a TJ-associated protein (Fig. 6D′). Thus, TJs appeared functional and are not the cause of WPB disruption in $CerS3^{d/d}$ mice.

Keratinocyte cornification is delayed

The transition of SG keratinocytes to corneocytes is precisely controlled accompanied by conspicuous morphological changes, including formation of a condensed cytokeratin filament network and CE parallel to degradation of nuclei, organelles and plasma membrane. To assess whether the final cornification arrest is triggered by a delay of earlier maturation steps, we analyzed the keratohyalin granule (KG)

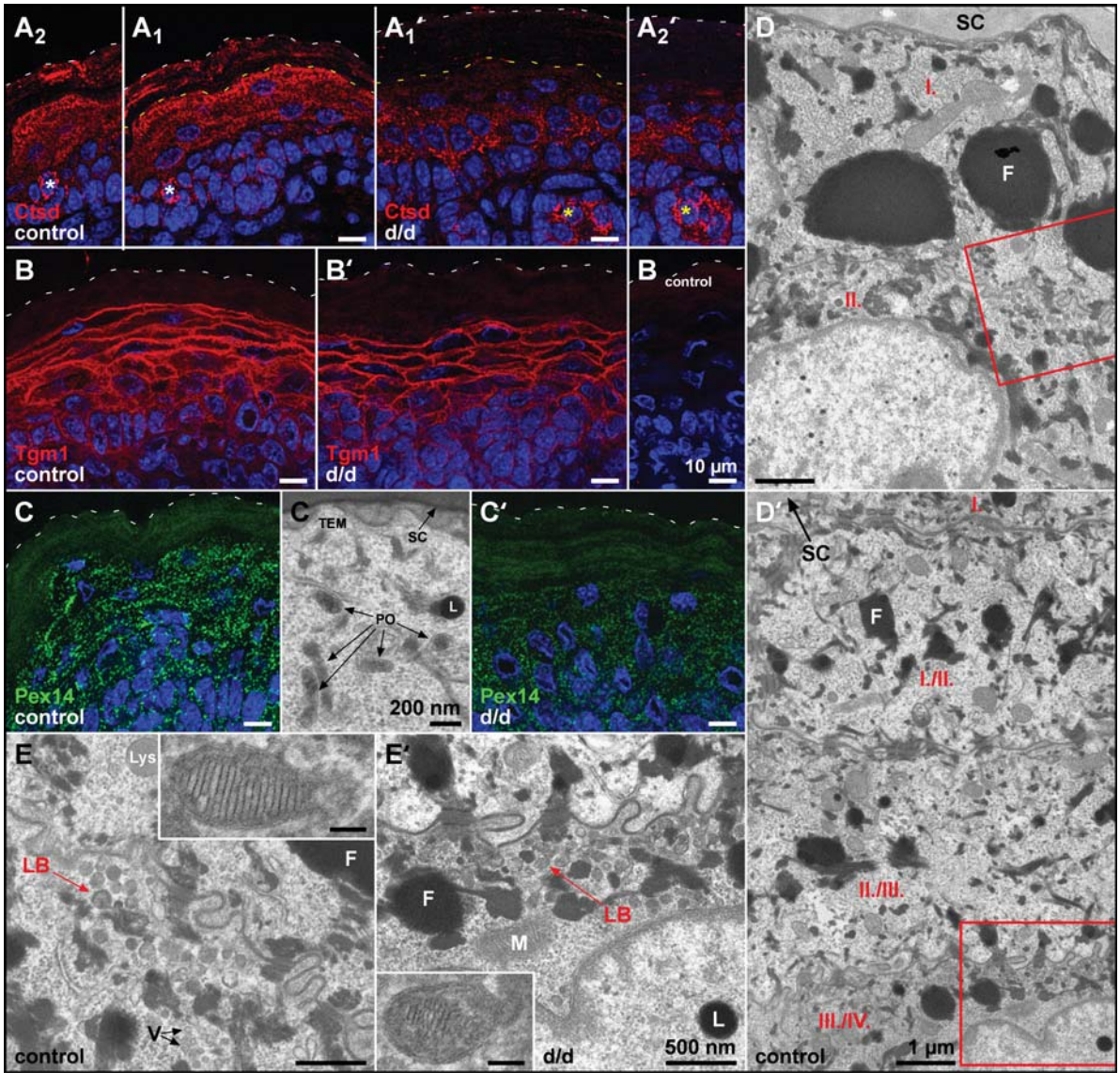

Figure 5. Establishment of a premature LB front. (**A** and A′) Consecutive skin sections (A_{1-2} and A'_{1-2}) reveal the front of Ctsd to appear about two layers earlier in mutants (lower SG) and positive labeling of SC only in control. Asterisks, corresponding hair follicles. (**B** and B′) *In situ* transglutaminase activity exhibits no distinct alterations between mutants and controls. (**C** and C′) Although the amount of Pex14 labeled peroxisomes is similar, staining intensity is drastically reduced in mutants. EM analysis reveals the tubulo-vesicular structure of catalase-positive peroxisomes (PO) (C_{TEM}, DAB/OsO_4). (A–C′) Nuclei, DAPI. (**D** and **E**′) EM confirms the front of unreleased LBs in the second SG layer in controls (D) and in the third/fourth SG layer in mutants. (E and E′) Higher magnifications of indicated frames in (D) and (D′) reveals slightly smaller size of mutant LBs, often containing shortened and fragmented lamellar stacks (inserts). OsO_4/tannin, F, filaggrin-containing F-granule; Lys, lysosome; L, loricrin-containing L-granule; M, mitochondria; V, small clear vesicles.

compartment. KGs were located within the SG and composed of large F-granules (profilaggrin) and small L-granules (loricrin). Mutants exhibited a marked reduction in size of KGs (Figs 2H–I′, 5D and D′ and 7A and A′). This decrease was already obvious at E18.5 (Supplementary Material, Fig. S2I–J′) and correlated with the reduced amounts of (pro)-filaggrin aggregates seen after immunolabeling (Fig. 7A and A′) and EM analysis (F in Figs 5D and D′ and 7E and E′). However, (pro)filaggrin labeling, which normally fades with cornification, was equally distributed within the entire mutant SC (Fig. 7A and A′).

Along with cornification, profilaggrin is proteolytically processed in its filaggrin units which function in keratin filament compaction. It is further degraded into free amino acids to moisturize SC (25). In mutant skin, this processing was quite insufficient as less monomeric, but much more trimeric and dimeric filaggrin units were present when compared with controls (Fig. 7F).

In line with a delay in cornification, the following observations were made: (i) F-actin persisted in the lower SC layers (Fig. 6B and B′), (ii) remnant nuclear material was detected in the first corneocyte layers after hemalaun, terminal deoxynucleotidyl transferase dUTP nick end labeling (TUNEL) (Supplementary Material, Fig. S4A′ and B′) and 4′,6-diamidino-2-phenylindole (DAPI) staining (Fig. 7D′), (iii) these lower SC layers exhibited residual glycogen (Supplementary

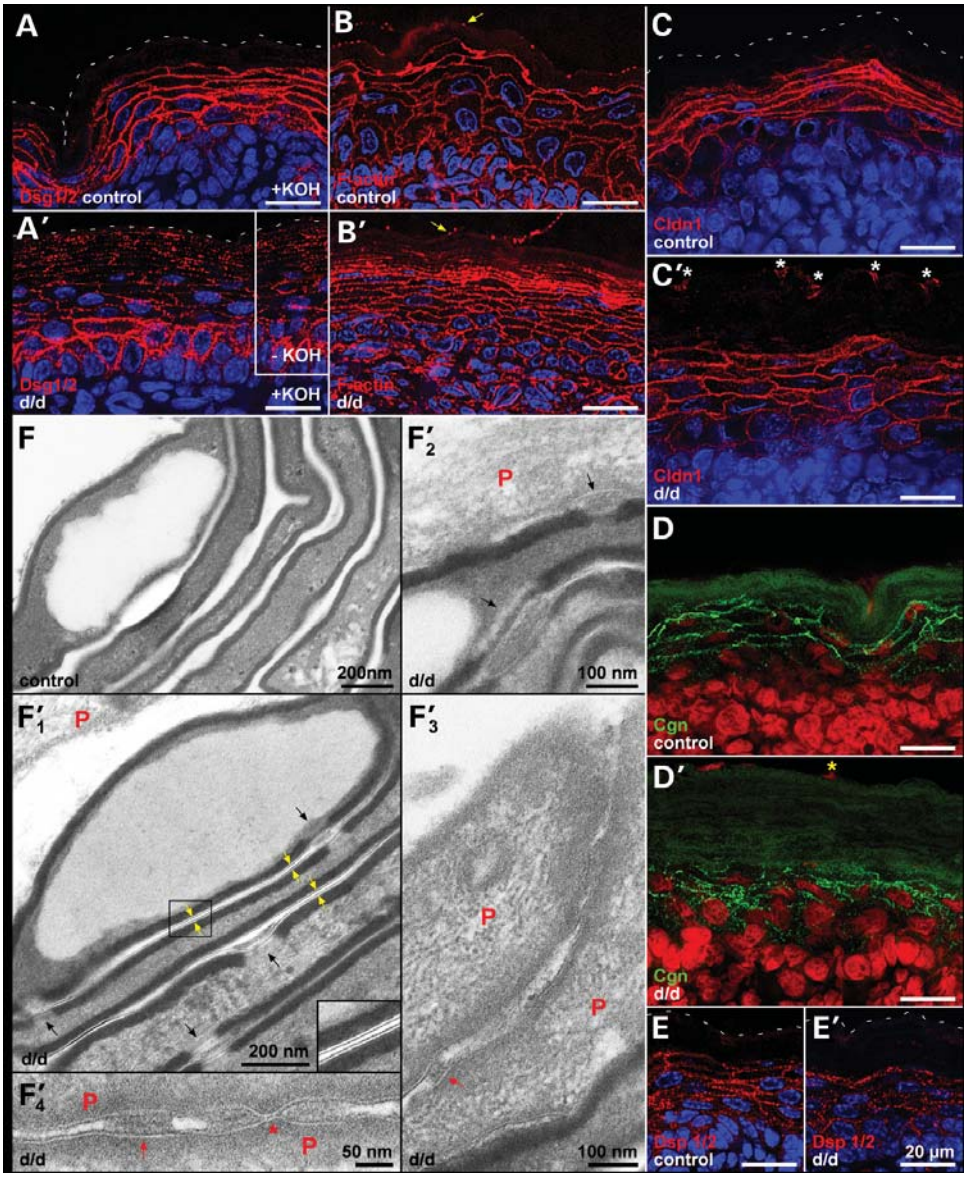

Figure 6. Abnormal SC cohesion and persistent periderm. (**A** and A′) Desmoglein 1/2 (Dsg1/2) reveals CD persistence throughout mutant epidermis, even without mild alkaline treatment (A′, insert). (**B** and B′) F-actin intensely decorates lower corneocyte layers only in mutants. F-actin-positive inclusion bodies delineate the outermost SC layer also in controls (yellow arrows). (**C** and C′) The distribution of claudin 1 (Cldn1) is similar, but in mutants SC surface is marked by peridermal TJs (white asterisks). (A–C′) Nuclei, DAPI. (D and D′) Cingulin (Cgn), a TJ-associated protein, exhibits linear strands within control SG which appear curled in mutants (**D**′). Yellow asterisk, peridermal nuclear remnant (Draq5). (**E** and E′) Distribution of desmoplakin 1/2 (Dsp 1/2), a desmosomal plaque protein, is not altered. Nuclei, DAPI. (**F** and F′) EM reveals a typical stratum disjunctum lacking non-peripheral CDs in the control upper SC, whereas in mutants a periderm persists (red P) equipped with TJs (F'_4, red asterisk, kissing points) and desmosomes ($F'_{3\text{-}}4$, red arrows). Cohesion between upper SC layers is guaranteed by non-peripheral CDs connecting also the periderm (F'_{1-2}, black arrows). Mutant upper corneocytes display trilaminar membrane structures (F'_1, yellow arrows and insert) indicating a phospholipid bilayer. Note the inclusion bodies of the superficial corneocytes in control and mutant. OsO_4/tannin.

Material, Fig. S4C′), restricted to viable layers in controls, and (iv) degradation of organelle structures within the first three SC layers was regularly incomplete in mutants (Supplementary Material, Fig. S4D′).

Late steps in CE assembly are impaired

Sequential CE assembly results in the formation of a highly insoluble, protective layer of proteins cross-linked to the keratin filament–filaggrin complex. Whereas involucrin and transglutaminase 1 expression mark early steps in CE assembly, one of the major CE proteins, loricrin, refers to late scaffold formation (26). To test whether CerS3 deficiency influences the expression pattern of early and/or late markers of CE assembly, we analyzed involucrin and loricrin localization by immunolabeling.

Involucrin appeared only slightly delayed in mutant SG (Fig. 7B and B′) and its total protein levels were not altered

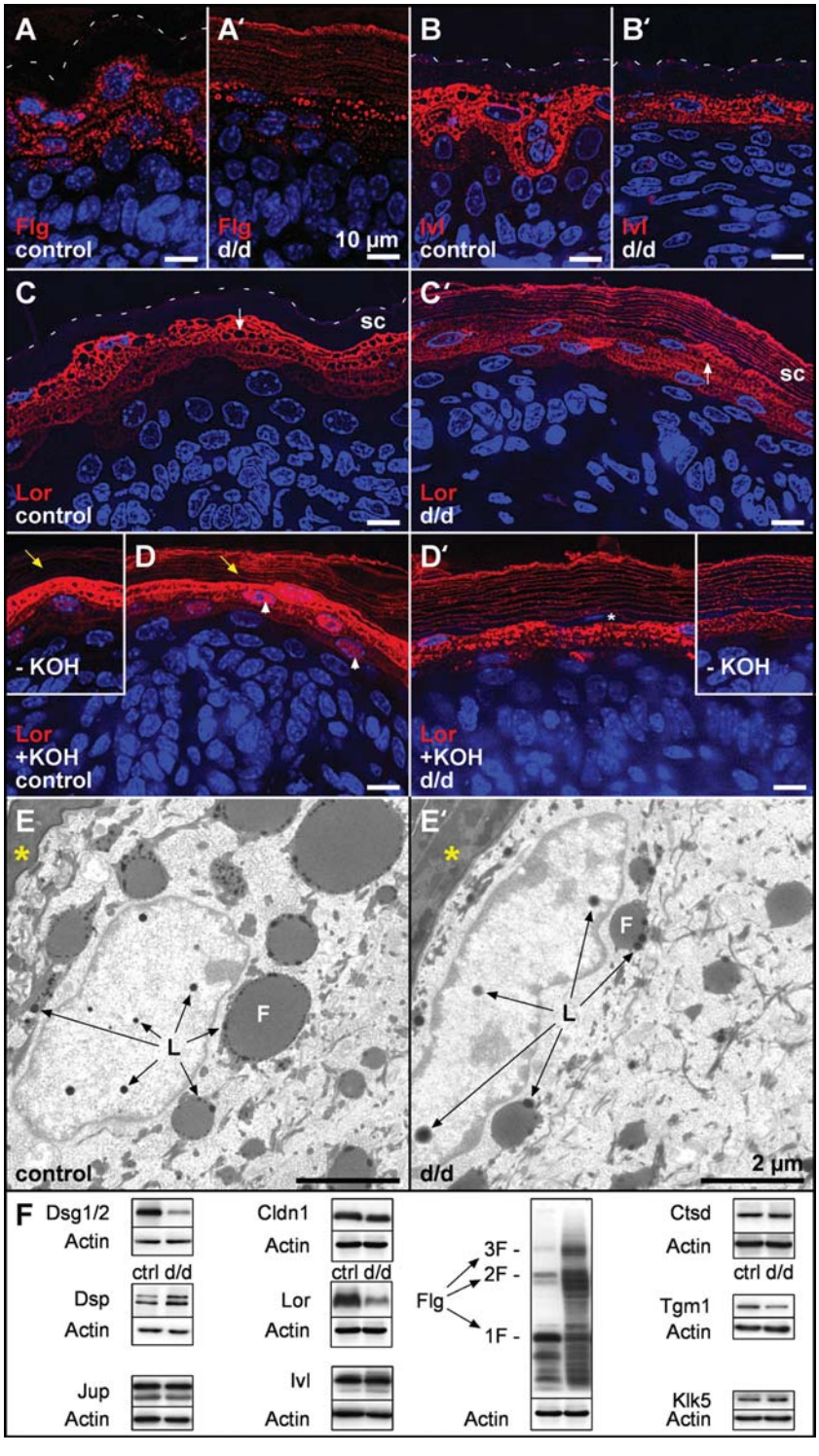

Figure 7. Impaired processing of epidermal proteins. (**A** and A′) In mutants, (pro)filaggrin (Flg) is weakly expressed within the lower SG, but the CE is intensely delineated. (**B** and B′) Involucrin (Ivl) is decreased in mutants. (**C** and C′) In cryosemithin sections, the increasing loricrin (Lor) signal decorating the rim of F-granules (white arrows) is obvious, but less intense in mutants. The latter show distinct CE lining. (**D** and D′) In paraffin sections, a faint loricrin staining appeared in control stratum disjunctum, but not in stratum compactum (D, insert). After alkaline treatment loricrin labeling strongly increased throughout SC, including stratum compactum in controls (yellow arrow). Note the reduced expression in mutant SG and the intense nuclear staining in controls (white arrowheads). White asterisk, residual nuclear DNA. (A–D′) Nuclei, DAPI. (**E** and E′) EM of the upper SG reveal in mutants a pronounced decrease in both the size of (pro)filaggrin-containing F-granules (**F**) and the number of loricrin-containing L-granules (L). The latter occur at the periphery of KGs and within the nucleus. Yellow asterisks, first corneocyte layer. DAB/OsO_4. (F) Immunoblots of the junction proteins desmoglein 1/2 (Dsg 1/2), desmoplakin 1/2 (Dsp1/2), plakoglobin (Jup), claudin 1 (Cldn1), CE proteins, loricrin (Lor) and involucrin (Ivl) as well as filaggrin (Flg), transglutaminase 1 (Tgm1) and the endoproteases Ctsd and Klk5. Equal loading was assessed by β-actin. Note, the deficient processing of profilaggrin into filaggrin monomers (1F) via trimers (3F) and dimers (2F). Blots shown are representative of at least three animals per group.

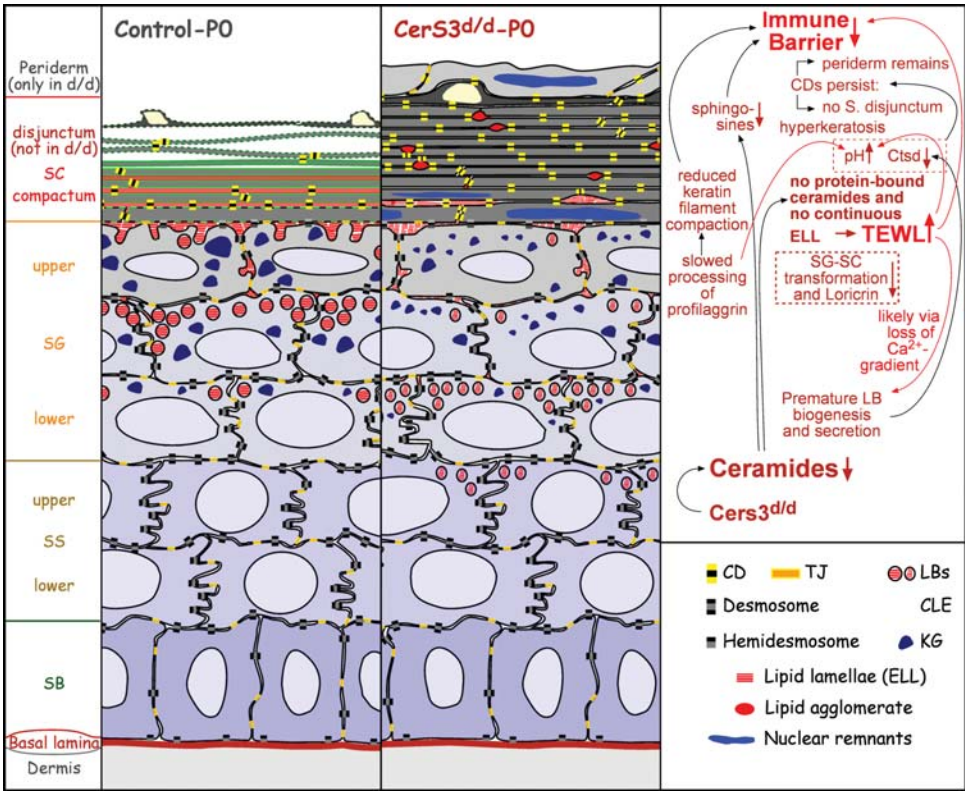

Figure 8. Schemes of CerS3$^{d/d}$ phenotypic alterations with proposed cascades of events.

(Fig. 7F). Considering the published covalent interactions of Cers with involucrin (27), we performed *in situ* methanolic mild alkaline treatment, but still did not visualize involucrin in the CE. Besides crosslinking CE proteins, membrane-anchored Tmg1 may esterify the latter, e.g. involucrin, with ωh-Cers. However, neither Tmg1 protein levels (Fig. 7F) nor transglutaminase activity *in situ* (Fig. 5B and B′) was altered.

At the EM level, loricrin granules distributed around the periphery of F-granules and within nuclei of granular keratinocytes. In mutants, their number and size were markedly reduced in both compartments (Fig. 7E and E′). These observations were confirmed by WB (Fig. 7F) and immunolabeling. Strikingly different, an intense loricrin staining was observed throughout mutant SC distinctly delineating CE (Fig. 7C and C′). We hypothesized that ωh-Cers esterify to loricrin in control SC to cover the epitope recognized by the antibody. If so, mild alkaline treatment hydrolyzing ester bonds should release the epitope in controls for detection of loricrin. Indeed, loricrin was observed under these conditions in controls in all SC layers and in particular in the SG nuclear compartment (Fig. 7D and D′). Hence, CerS3 deficiency impaired late steps in CE assembly.

We summarized the phenotypic alterations in mutant epidermis and propose a sequence of events in Figure 8.

DISCUSSION

Investigating the recently discovered mammalian CerS family, we addressed whether a specific CerS is required for biosynthesis of Cers with ULC-FAs, to which epidermal ωh-Cers belong. Exclusively, CerS2 and CerS3 have been reported to prefer the longest acyl-CoAs (≤C26) tested in cell lysates (11,28). Using transfected HeLa cells and mutant yeast strains, we provide evidence that CerS3 is the only mammalian CerS capable of converting ULC-acyl-CoAs into Cers. In addition, CerS3 uses VLC- and LC-acyl-CoAs, reflecting its wide substrate specificity. Hence, a combination of CerS3 with a special acyl-CoA pool is required to explain the unique epidermal Cer pattern observed.

To assess the consequences of CerS3 dysfunction on epidermal barrier properties and structure, we eliminated exon 7 in mice which contains the first conserved amino acids of the catalytic LAG domain (29). More importantly, exon 7 codes by computational prediction for a complete transmembrane domain. Thus, the remaining protein, if expressed, would have altered membrane topology. This systemic mutation resulted in complete loss of Cer-based SLs having acyl moieties of 26 or more carbon atoms in epidermis verifying absence of CerS3 activity and confirming *in vivo* that CerS3, but no other CerS, is required for ULC-Cer synthesis. SL deficiency includes those with non-, α- or ω-hydroxy-acyl moieties with or without double bonds from Δ^{15}-position onwards, pointing out a quite non-specific recognition related to acyl-CoA modifications. Furthermore, SLs with C22/24-acyl moieties are significantly reduced, validating in mice CerS3 substrate promiscuity as for acyl-CoA length. As VLC-acyl-CoAs with C22–C26 are preferred substrates of CerS2, absence of C26 and reduced C22/C24-SLs in CerS3-deficient epidermis suggest lack of CerS2 expression in

granular and upper spinosum keratinocytes, where we find CerS3 to be localized in controls. Hence, absence of epidermal VLC/ULC-SLs results in a lethal WPB breakdown. A similar WPB disruption leading to murine neonatal death has been reported for genetic mutations affecting acyl-precursor synthesis, esterification and processing of Cers or intracellular lipid transport (30–32). In humans, corresponding mutations underlie, i.e. severe harlequin ichthyosis, Dorfman–Chanarin syndrome, ichthyosis prematurity syndrome and Gaucher disease (collodion babies) (33–36). Although not mentioned, published photos of Elov4-, Cgi-58- and ABCA12-deficient mice suggest also absence of feeding in these strains (37–39). It may be questioned if neonatal skin barrier disruption generally alters odor signals responsible for maternal recognition and nursing (40–42).

Using cultured neonatal skin inoculated with *C. albicans*, we demonstrated that the loss of VLC/ULC-SL compromises the cutaneous barrier against pathogens. Rather than altered antimicrobial peptides, the following factors may facilitate *C. albicans* invasion: (i) increased water flux across the deficient WPB enhancing SC hydration, (ii) impaired keratin filament compaction through insufficient filaggrin processing likely accelerating proteolysis for penetration, (iii) residual periderm improving adhesiveness, and (iv) loss of Cer downstream products *per se* possessing potent antimicrobial properties. Indeed, the bioactive SLs, sphingosine and phytosphingosine generated from Cers during final cornification are natural antimicrobial agents, preventing *Staphylococcus aureus* infection or growth of *C. albicans* (4,5,7). In CerS3-deficient epidermis, Cers are basically absent and sphingosine levels drop to very low levels. Our data underscore a dual, indispensable function of Cers in skin. They serve as mortar in WPB maintenance and as a superficial coat for anti-microbial defense, the latter via sphingosine.

The structural basis for barrier disruption can be clearly attributed to the presence of ELL-free intercellular domains already occurring at the interface and throughout SC. Thus, sealing of the extracellular space is strikingly insufficient and ELL-free domains may operate like pores of a sieve mediating excess paracellular water and electrolyte loss, thereby disrupting the highly regulated pH and/or Ca^{2+} gradient across SC. It may be noted that ULC-Cers, completely missing in mutants, apparently are not a prerequisite of ELL formation, although the ordered structures are restricted to specific domains between the lower two to three SC layers. However, in upper SC the residual, incomplete lipid mixture, basically composed of cholesterol and free FAs, is compacted to focal agglomerates indicating impaired CLE formation. One could speculate that the absence of protein-bound Cers at the CE surface is the driving force of lipid cluster formation. Increased hydrophilic surface properties of opposing corneocytes due to insufficient CLE formation may favor their approximation pushing remaining extracellular lipids to fuse into agglomerates. Hence, an intact CLE would serve as ‘chaperone’ for even spreading of ELL and/or as cohesion/stabilizer of ELL. Our findings underscore the essential role of VLC/ULC-Cers in proper CLE formation required for organization and maturation of the extracellular lipid system. Consequently, a decrease in the total Cer content necessarily results in diminished barrier function as seen in many human skin disorders (2,43–45).

Although protein-bound ωh-Cers were missing in mutants, an electron-dense CE beneath the plasma membrane appears unaltered ultrastructurally. Following the labeling of loricrin, a major CE compound comprising up to 85% of the CE proteins (46), we document loss of ULC-Cers to be responsible for unmasking of loricrin throughout the mutant SC. Like involucrin, loricrin is not recognized within control SC by most antibodies due to posttranslational processing (47,48). As we could release the hidden loricrin epitope in control CE upon alkaline treatment, but did not uncover involucrin, it appears plausible that the epitope recognized in loricrin is an esterification site for ωh-Cers but not for other CE proteins. This suggests an important role in CLE formation for loricrin, a late component in CE assembly. It offers a suitable tool to unveil abnormalities of the cutaneous extracellular lipid system on sections from patients with skin disorders.

Unravelling the effects of ωh-Cer deficiency on epidermal morphology in more detail, we demonstrate further conspicuous phenotypic alterations including accelerated LB formation and release, hyperkeratosis, abnormal SC cohesion, maintenance of the trilaminar plasma membrane structure of corneocytes and persistent periderm, all of which reflect impaired cornification.

Regarding the LB secretory system in mutants, we documented a conspicuous shift of the LB front one to two cell layers earlier which may result from increased water flux. The latter destroys the epidermal calcium gradient triggering accelerated LB synthesis and extrusion (17). This in turn leads apparently to incomplete packing of other target components, such as Ctsd which exhibits a drastic decrease in SG labeling intensity and is nearly absent in SC.

Although LB formation and secretion appear accelerated, we observed a general maturation delay of corneocytes. In line with this delay, profilaggrin-containing KGs display a small, immature size even in the uppermost SG layer and processing of profilaggrin into monomers is retarded as residual monomers/multimers are easily recognizable in mutant SC. Before being proteolytically degraded into individual amino acids, profilaggrin is cleaved into filaggrin monomers. They crosslink keratin filaments to each other and to the CE, a process required for keratin filament bundling and compaction (25). Lower monomer levels thus will hinder condensation of corneocytes as observed throughout mutant SC.

A processing defect of profilaggrin into filaggrin monomers has been described in mice and humans with mutations in the filaggrin gene being associated, i.e. with atopic dermatitis (49). Here, we show delayed filaggrin processing may not necessarily result from filaggrin gene mutations, but may derive from lipid barrier abnormalities.

Further evidence for deficient cornification is reflected by persistence of corneocyte trilaminar plasma membrane structures and non-peripheral CDs. The latter are not only seen in stratum compactum like in controls, but up to the top of mutant SC, and hinder transition of stratum compactum into stratum disjunctum. Although plaque proteins, e.g. desmoplakin 1/2 likely, are degraded in control and mutant SC, the cytosolic domain of desmoglein 1 is preserved throughout mutant, but not control SC. This is in line with deficient extracellular processing of the desmosomal core containing the extracellular domains of desmoglein 1. CD retention may be

Table 1. Primers used for the generation of expression constructs

Plasmid	Primer sequence		T_1, T_2[a] (°C)	Product size (bp)
mCerS3-EGFP	F[b]	5′-ATG TTT CAG ACG TTT AGA AAA TGG TT-3′	56, 56	1171
	R[b]	5′-CGC CAC ATT GTG CTT CAA-3′		
	F	5′-TAT ATA GAA TTC GCC ACC ATG TTT CAG ACG TTT AGA AAA TGG TTC TGG-3′	56, 62	1181
	R	5 ′-TAT ATA GGA TCC GTA CGG CCA TGC TGA CCA TTG GCA ATG-3′		
hCerS2-EGFP	F	5′-CAG GAT GCT CCA GAC CTT GT-3′	53, 53	1164
	R	5′-GCA GCT GGA ATA ATG GTT CA-3′		
	F	5′-TAT ATA AAG CTT GCC ACC ATG CTC CAG ACC TTG TAT GAT TAC TT-3′	54, 62	1171
	R	5′-TAT ATA GAA TTC GGT CAT TCT TAC GAT GGT TGT TAT TGA GGA TG-3′		
pRevTRE2-mCerS3-EGFP	F	5′-TAT ATA GGA TCC GC CAC CAT GTT TCA GAC GTT TAG AAA ATG GTT CTG G-3′	56, 66	1181
	R	5′-TAT ATA ACC GGT GTA CGG CCA TGC TGA CCA TTG GCA ATG-3′		
pRevTRE2-hCerS3-EGFP	F	5′-TAT ATA GGA TCC GCC ACC ATG TTT TGG ACG TTT AAA GAA TGG TTC TGG-3′	56, 66	1181
	R	5′-TAT ATA ACC GGT GTA TGG CCA TGC TGG CCA TTG GGA ATG-3′		

Restriction sites are underlined.
[a]T_1 corresponds to the annealing temperature used for the first 10 cyles, T_2 corresponds to the annealing temperature used for the following 15 cycles.
[b]F, forward primer; R, reverse primer.

attributed to lowered protease activities arising from increased pH and inadequate protease secretion. Here, we show reduced Ctsd labeling of SC. Ctsd is involved in CD degradation (21) and requires an acidic pH for optimal activity (50). Skin hydration directly regulates SC pH. Disruption of the WPB leads to increased release of interstitial fluid with a neutral pH counteracting acidification of the skin. Additionally, the increased pH may be attributed to decreased histidine-to-urocanic-acid generation as a matter of insufficient filaggrin breakdown (22) and/or dysfunction of secretory phospholipase A2 generating free FAs as well as decreased activity of the sodium-proton exchanger, type 1 (NHE1) (51). Increased SC pH in turn may also contribute to a residual phospholipid bilayer due to lowered lipase activities. Interestingly, CD persistence is also a characteristic feature of ichthyosis and xerosis combined with hyperkeratosis (52).

Cohesive CDs may also be responsible for postnatal persistence of periderm and maintenance of its intercellular junctions (desmosomes and TJs). This embryonic structure shed before birth in controls is very sensitive to mechanical stress and therefore easily detached, leaving traces of cell debris. Indeed, residual nuclear DNA on top of SC is described in Abca12-deficient mice, but discussed as parakeratosis (53). However, nuclear staining within SC is not detectable. These topical nuclear remnants may derive alternatively from residual periderm. It is questionable whether a persisting, but not recognized periderm exists in published mouse models presenting similar barrier defect and morphological phenotype, e.g. as documented for Elovl4-deficient mice in Figure 4B (54).

In conclusion, CerS3 is essential for the synthesis of CLE- and ELL-Cers and importantly for Cer-derived sphingosines. Hence, CerS3 determines the quality of WPB and antimicrobial function as well as final cornification. Currently, no monogenetic human skin disease associated with *CERS3* has been identified. As mutations may lead to impaired barrier function irreplaceable by other CerS, the phenotype expected may be related to atopic dermatitis, ichthyosis or psoriasis. Paradigmatically, in a large cohort of families affected by autosomal recessive congenital ichthyosis, 78% of all cases could be linked to established gene mutations, i.e. in FLG, ABCA12 or TGM1. For 22%, the affected gene remained to be identified. Interestingly, mutations in 12 of at least 34 genes directly affect lipid metabolism (55). In addition, considering sphingosine as an important component of the antimicrobial barrier and innate skin immunity, i.e. chronic mucocutaneous candidiasis disease, for which in most cases the underlying etiology is still unknown (56,57), offers a potential linkage to the *CERS3* gene. As CMC represents a prominent feature in severe atopic dermatitis (58) associated with 2-fold reduction in SC sphingosines (4) screening for mutations of *CERS3* in affected families may be considered. Finally, the important role of SLs in atopic dermatitis had been underlined by the beneficial topical application of a ceramide-dominant mixture as exemplified in reference (59), which independently of the utilized ceramide species should release antimicrobial sphingosine.

MATERIALS AND METHODS

Generation of CerS3 and CerS2 expression plasmids

Mammalian expression plasmids encoding for either human CerS2 or mouse CerS3 were generated by cloning of *Cers2* (officially longevity assurance homolog 2, *Lass2*) or *Cers3* (*Lass3*) cDNA into the N-terminus of an EGFP taq vector. Thus, cDNA isolated from the kidney (for CerS2) and testis (for CerS3) was amplified by PCR using specific primers (see Table 1 for primer sequences and temperature conditions). For CerS3, a DNA fragment including exons 2–11 but excluding exon 1, which is absent in the human protein, was used for cloning. The amplified DNA fragments were then inserted into pEGFP-N1 (Clonetech) vector by *Hin*dIII/*Eco*RI or *Eco*RI/*Bam*HI sites for CerS2 and CerS3, respectively. Following DNA digestion of the corresponding inserts and

vectors, these were subsequently ligated to generate hCerS2-EGFP and mCerS3-EGFP.

For retroviral transduction, mCerS3-EGFP and human CerS3 plasmids (EX-T7111-M02, Genecopoeia) were further subcloned into pRevTRE2-EGFP. Both genes were inserted using primers flanked with *Bam*HI and *Age*I sites.

All PCR products were generated using *Pfu* polymerase (Promega). The sequences of all constructs were verified by DNA sequencing.

Generation of stable cell lines expressing CerS3

Stable cell lines expressing CerS3-EGFP (mouse and human), as well as EGFP (control), were generated by retroviral transduction using genetically modified HeLa cells ($HeLa_{mCAT1\text{-}rtTA2\text{-}M2}$). Previous integration of mCAT1 (murine cationic amino acid transporter 1) and the doxycycline-sensitive transactivator rtTA2-M2 (optimized reverse tetracycline-controlled transactivator) allowed the generation of inducible HeLa cells expressing the gene of interest, as already described (60). Briefly, viral particles required for transduction were produced in the capsid-forming cell line HEK-293T. These virions were generated via the triple transfection with (i) a MoMLV (Moloney murine leukemia virus) derived retroviral vector encoding CerS3 from the doxycycline/transactivator responsive element (pRevTRE2-CerS3-EGFP or control pRevTRE2-EGFP), together with (ii) *gag-pol* (pVPack-GP) and (iii) *envelope* (pVPack-Eco). The latter vectors are both responsible for the formation of viral proteins. MBS mammalian transfection kit and pVPack vectors were used according to the manufacturer's recommendations (Stratagene). Following 48 h transfection, virions were collected and used to transduce target cells. After 40 h incubation with 2 μg/ml doxycycline, fluorescent-positive cells were isolated by fluorescence-activated cell sorting. These populations were cultured for 7 days in the absence of doxycycline and then selected for negative fluorescence signals. Following an additional 7 days induction with doxycyline, single cell clones were sorted by EGFP-derived fluorescence. HeLa cell lines expressing mCerS3-EGFP, hCerS3-EGFP and control EGFP were generated according to this procedure.

Chemical synthesis

Montanoyl(C28:0)-CoA. For activation of the carboxylic acid, montanic acid (28:0, 100 μmol, Sigma) was dissolved in tetrahydrofuran (4 ml, Fluka). Equimolar amounts of *N*-hydroxysuccinimide (Fluka) and dicyclohexylcarbodiimide (Fluka) were added at room temperature (RT) and the reaction was kept under nitrogen for 12 h. The activated FAs were coupled to the polysilylated form of coenzyme A, which was generated *in situ* as previously described with slight modifications (61). Thus, the trilithium salt of coenzyme A (American Radiolabeled Chemicals) was passed through a Dowex-50 ion exchange column acidified with 1 M HCl and subsequently lyophilized. The resulting free CoA (26 μmol) was dissolved in dry acetonitrile (2 ml, Fluka). Dimethylketene methyl trimethylsilyl acetal (650 μmol, Sigma) was added and the resulting solution was stirred for 16 h under nitrogen. After removal of all volatiles using a nitrogen stream, the polysilylated coenzyme A was dissolved in 1 ml of dry tetrahydrofuran. To a stirred solution of activated FA (39 μmol) in tetrahydrofuran containing CsF (1.3 mmol, Fluka) and dicyclohexano-18-crown-6 (0.13 mmol, Fluka), the coenzyme A solution was added drop-wise and the reaction mixture was stirred for 4 h at RT. The crude mixture was acidified with an equal volume of 10 mM KH_2PO_4 (pH 5.5), and the organic solvent was removed using a nitrogen stream. The aqueous phase was desalted using a reverse phase C18 column and the final product was eluted with methanol. For quantification, MS analyses with acyl-CoAs of known concentrations were performed.

Ceramide internal standards for electrospray-ionization tandem-MS. FAs were activated into their respective *N*-hydroxysuccinimide esters as reported above, and then condensed (40 μmol each) with d17:1-sphingosine (10.5 mmol, Avanti Polar Lipids) in a final volume of 4 ml tetrahydrofuran. The reaction was catalyzed by triethylamine (Sigma) for 1–2 days at RT in an inert atmosphere. The crude products were purified by silica gel flash-column chromatography using mixtures of hexane/isopropanol/water of increased polarity as solvent system. For quantification, a dilution series of the purified products were spotted on a high-performance TLC (HPTLC) together with standards of known concentration and separated with the cloroform/methanol/acetic acid (188/11/1). After development with 10% copper (II) sulphate in 8% sulphuric acid (10 min at 180°C), quantification of the bands was performed by densitrometric scanning using a TLC scanner (Shimadzu CS-9301).

ULC-CoA specificity assay of CerS2 and CerS3

Living mammalian cells. HeLa cells stably transfected with mouse and human CerS3, EGFP control, as well as *untreated* cells ($HeLa_{mCAT1\text{-}rtTA2\text{-}M2}$) were seeded onto six-well plates with a density of 1×10^5 cells/well with or without induction with 2 μg/ml doxycycline. Forty-eight hours after seeding, *untreated* cells were transfected with hCerS2-EGFP and incubated for 4 h at 37°C. The assay was started by exposing the cells to media containing a mixture of saturated acyl-CoAs, namely C16:0, C18:0, C24:0, C26:0 (Avanti Polar Lipids) and C28:0 (10 μM each) and 6 μM sphingosine (d17:1). Upon 20 h of reaction, cells were harvested and lipids extracted. Uptake only occurred in the presence of the crude montanoyl CoA (as described), with no incorporation using HPLC-MS purified C28:0-CoA.

Yeast. The strains used for this assay were the following: RH2888 (*MATa his3 leu2 lys2 trp1 ura3 can1 bar1*), RH6974 (*MATα FLAG-MmCerS2::TRP1 lac1Δ::ADE2 lag1Δ::HIS3 leu2 ura3 lys2 can1 bar1*) and RH6975 (*MATα FLAG-HsCerS3::TRP1 lac1Δ::ADE2 lag1Δ::HIS3 leu2 ura3 lys2 can1 bar1*). All mutations were constructed using standard gene disruption procedures, with complete removal of open reading frames in the RH2888 strain background. Double and triple mutants were obtained by genetic crosses. Synthetic N-terminally FLAG-tagged (FLAG-tag sequence: N-DYKDDDDK-C) open reading frames corresponding to mouse CerS2 and human CerS3 were purchased from

Table 2. Primers used for the generation and genotyping of CerS3$^{d/d}$ mice

Gene	Primer sequence		T_a (°C)	Product size (bp)
Primers used for Southern blot				
5′ probe	F	5′-TGA CAA CCC CAC TGC AAA ACT-3′	58	557
	R	5′-ATC CCA GCT TGT GGA TGG ATT-3′		
3′ probe	F	5′-AAT GAA TGC TTC TGC CTT TCC A-3′	58	506
	R	5′-TGG GAG AGG AGC CTC ACT ACA G-3′		
Primers used for genomic DNA genotyping				
*CerS3*Δexon7	F	5′-ACA TAT CTC CCT TTG CCC TGA TG-3′	58	1004[a], 272[b]
	R	5′-GAC AGC CCT GAA ATG TAT CAT GC-3′		
Primers used for cDNA genotyping				
CerS3-ex6-11	F	5′-TCT GGG AGG TTT GGA ATG AC-3′	55	687[a], 594[b]
	R	5′-CGC CAC ATT GTG CTT CAA-3′		
Primers used for quantitative RT–PCR				
RT-*CerS3*Δex7	F	5′- GGT CAC TGG TGT TTA GCC TGA-3′	55	128
	R	5′-GGT CCC ACT GCG AAT GTA AT-3′		

[a]Product size for wild-type *CerS3* allele.
[b]Product size for mutant *CerS3* allele.

GeneArt (Germany) as yeast codon optimized open reading frames, subcloned for expression under control of a *TDH3* promoter and inserted into the genome to construct stable cell lines. Sequences are available upon request.

For CerS assay *in vivo*, hCerS3 and mCerS2 expressing strains deleted for the yeast ceramide synthases, *LAC1* and *LAG1*, and control yeast strains were transformed with the wild-type or mutated Sur4 protein (F262A/K266L, kind gift from J. Weissman) (14). Yeast was grown on SD medium with the required nutrients to a final concentration of 1 OD_{600}/ml and lipids were extracted from 50 ml of cells as described below.

Generation of CerS3$^{d/d}$ mice

The *Cers3* gene (ceramide synthase 3, *Lass3*, NCBI gene ID: 545975) was found in a mouse C57Bl6 bacterial artificial chromosome (BAC) Library (RPCI-23 No. 731, German Resource Center for Genome Research, RZPD). From the corresponding BAC-DNA clone, a ~10 kb *Xba*I/*Xho*I fragment including exons 5–9 of *Cers3* was subcloned into a pBluescript plasmid vector (Stratagene). An HSVtk-PGKneo cassette flanked by two FRT, one 5′-single loxP side and a diagnostic SacI side was cloned into ClaI in introns 6–7. A single loxP site was inserted into SpeI of introns 7–8. A PGK-DTA cassette was inserted into *Xho*I at the 3′ end of the targeting construct. E14 ES cells derived from mouse strain 129 SV Ola were transfected in the presence of the linearized *Cers3*-targeting vector. Stem cell clones were picked, expanded and checked for homologous recombination of *Cers3* by Southern blot analysis. Genomic ES-cell DNA was digested with SacI and a digoxigenin labeled 3′-outside probe (Roche) was used to stain wild-type and mutant alleles. No positive clone could be detected out of 384 cultivated. Sequence analysis of the C57Bl6 mouse line-derived targeting vector DNA resulted into pronounced variations in particular within intron 5 of the 5′ region of the targeting construct when compared with 129 SV Ola DNA from which mouse strain stem cells were derived. Therefore, the 5′ arm of the targeting construct was replaced by a PCR product amplified with a proofreading polymerase from a genomic 129 SV Ola DNA. Sequence analysis of the changed targeting construct showed a correct *Cers3* sequence for all exons, including the 129 SV Ola derived 5′-arm. As verified by Southern blot analysis, electroporation with the reconstructed vector resulted in two clones out of 384 with correct 5′ insertion of the targeting construct, including the selection cassette with 5′ loxP side. Only one of the respective ES clones showed an integration of the single loxP site 3′ from exon 7. Stem cells from the latter clone were expanded and injected into blastocysts. Germline transmission of mutant stem cells was achieved, indicated by agouti colored offspring from chimeras. F1 offspring with loxP-flanked exon 7 were further mated with cre-deleter mice to obtain a systemic deletion of exon 7 of the *Cers3* gene. In the next breeding step, the cre-transgene was again removed by mating with C57Bl6 wild-type mice. Heterozygous mice were mated in order to generate homozygous offspring with complete exon 7 deletion in *Cers3* in both alleles.

All animal procedures were approved and performed in accordance with federal laws (Regierungspräsidium Karlsruhe, Germany, G-68/07, G-8/07 and A-62/06).

Genotyping of mutant mice

ES cells, F1 offspring and mutant mice were genotyped by Southern blot and PCR analyses. The 3′ and 5′ Southern probes were synthesized using the PCR DIG probe synthesis kit, essentially according to the manufacturers protocol (Roche). For PCR analyses, either genomic DNA isolated from mice tails or cDNA isolated from skin were used as templates to amplify specific products for wild-type and mutant alleles. Primers used to perform these analyses including the corresponding conditions are specified in Table 2. The generation of the truncated *Cers3* transcript lacking exon 7 in mutant mice was confirmed by DNA sequencing.

RNA isolation and quantitative real-time PCR

Neonatal CerS3$^{d/d}$ and littermate control skin was collected to compare relative mRNA expression levels of CerS

Table 3. Primers used for qRT–PCR of antimicrobial peptides

Gene	Primer sequence		T (°C)	Product size (bp)
mBD1/Defb1	F	5′-GGT GTT GGC ATT CTC ACA AGT C-3′	60	99
	R	5′-GGT ATT AGA TGG GCA GCT GGA G-3′		
mBD2/Defb2	F	5′-TGC TGC CTC CTT TTC TCA TAT ACC A-3′	60	78
	R	5′-GTG GTC AAG TTC TGC TTC GTA TC-3′		
mBD3/Defb3	F	5′-ATG CTG GAA TCG GTG CAT TGG CA-3′	64	138
	R	5′-CTT CAT GGA GGA GCA AAT TCT GGT GT-3′		
mBD4[a]*/Defb4*	F	5′-CAC ATT TCT CCT GGT GCT GCT-3′	64	52
	R	5′-GAT AAT TTG GGT AAA GGC TGC AA-3′		
mCamp	F	5′-CTT CAA CCA GCA GTC CCT AGA CA-3′	60	53
	R	5′-GAT CCA GGT CCA GGA GAC GGT A-3′		

[a]BD4 primer sequence reported by Dorschner *et al*. (76).

homologues and antimicrobial peptides. Total RNA was extracted using Trizol reagent (Invitrogen) according to the manufacturer's instructions, following integrity assessment using RNA6000 Nanochip (Agilent). Double-stranded cDNA was synthesized and evaluated for relative gene expression as previously described (13). Results represent the fold-change of expression calculated using the comparative C_t method. Normalized ΔC_t values were compared with normalized ΔC_t of wild-type *mCers5*- and *mCamp*-mRNA for quantification of *Cers*- and antimicrobial peptide-mRNAs, respectively. Primers used for enhancing specifically each *Cers* homologue were as reported (13), with the exception of *Cers3*, where primers within exons 7 and 8 were used and are indicated in Table 2. Primers used for quantitative reverse transcription polymerase chain reaction (qRT–PCR) of antimicrobial peptides and the corresponding specific conditions are detailed in Table 3.

Skin permeability assay

Skin permeability was tested by diffusion using Mayer's hemalaun essentially as described (38). In brief, euthanized embryos and newborn animals were fixed in methanol for 5 min, washed with phosphate-buffered saline (PBS) and incubated in Mayer's hemalaun (Roth) for 20–30 min at RT. Excess hemalaun was removed by several thorough washes with PBS. After hemalaun staining, images of the animals were captured using a digital camera.

Determination of TEWL and epidermal pH

TEWL was measured using a Tewameter TM300 (Courage-Khazaka Electronics) as described (48).

Preliminary skin surface pH measurements were performed using humidified pH-indicator strips (pH 5.2–7.2, Merck).

Candida albicans infection of cultured skin samples

Interscapular skin samples of newborns were maintained viable on collagen gels partially submerged in the Dulbecco's modified Eagle's medium (DMEM) (Lonza, BE12-604F) supplemented with 50 U/ml penicillin and 50 μg/ml streptomycin (Gibco). Collagen gels were prepared as previously described (62). Thus, type I collagen was isolated from tail tendons of young rats and lyophilized. To a 4 mg/ml solution of collagen in 0.1% acetic acid was added 10% of 10× Hank's balanced salt solution (Gibco) titrated with 5 M sodium hydroxide and 10% of the DMEM medium. The mixture was allowed to jellify in PET membrane filter inserts (Falcon) for 1 h at 37°C, following the addition of 12 ml DMEM medium in each of the deep-wells (BD Biosciences, BD 355467).

Candida albicans (ATCC 90028) grown overnight in the LB medium were harvested and resuspended in PBS to a concentration of 10^9/ml. *Candida albicans* (1×10^6 cells, 1 μl) were inoculated to the center of the skin sample and incubated at 30°C for the specified time.

For quantification of microbial growth, infected skin samples from E18.5 ± 0.5 mice were flushed with 10 ml PBS. An aliquot of these suspensions (100 μl) were plated in two different dilutions on Sabouroud agar plates (bioMérieux). Multiple serial dilutions had been previously performed to determine optimal conditions. After 24 h incubation at 37°C, colonies were counted and concentrations were determined as colony forming units (CFU/ml).

Lipid extraction

For the extraction of epidermal lipids, interscapular skin samples were rapidly dissected and snap-frozen in liquid nitrogen. To separate epidermis from dermis, samples were treated with 500 μg/ml thermolysin buffer (containing 10 mM 4-(2-hydroxyethyl)-1-piperazineethanesulfonic acid (HEPES), 142 mM NaCl, 6.7 mM KCl, 0.43 mM NaOH, 1 mM $CaCl_2$ at pH 7.4) for 2 h at 37°C (63). Isolated epidermis was then cut into small pieces and lyophilized. SLs were extracted according to Doering *et al*. with slight modifications (48,64). In brief, ∼3 mg of dry weight epidermis was extracted with 2 ml of chloroform/methanol/distilled water 30/60/8 by volume at 50°C for 15 min under sonication. Supernatant was taken after centrifugation and pellets were re-extracted two additional times using the solvent mixtures of chloroform/methanol/distilled water, 10/10/1, and chloroform/methanol, 2:1 by volume. Supernatants were pooled and desalted using reversed phase RP-18 columns. For further analysis, aliquots of the extract pool were saponified under mild alkaline conditions (0.1 M methanolic KOH, 4 h, 50°C), neutralized with acetic acid and desalted using 100 mg-RP-18

columns. Protein-bound SLs were extracted from the above obtained pellets. Pellets were 'washed' three times with 2 ml of 100% methanol for 5 min and two times with 2 ml of 95% methanol at 60°C for 2 h to remove residual-free lipids. Treatment of the residual pellets with 1 ml of 1 M KOH in 95% methanol at 60°C for 2 h cleaved ester linkages and released protein-bound SLs. Supernatants were neutralized with acetic acid and desalted using RP-18 columns as above.

For the extraction of SLs from HeLa cells, dried cell pellets were extracted twice with 2 ml of chloroform/methanol/distilled water, 10/10/1 and once with 30/60/8 (by vol.) for 15 min at 37°C. Combined lipid extracts were subjected to methanolic mild alkaline hydrolysis for 2 h at 37°C, sequentially neutralized and desalted.

For the extraction of yeast lipids, internal standards were added to the samples (10 μg each of Cer (d18:1,17:0) and GlcCer (d18:1, 8:0), Avanti Polar Lipids), which were then extracted using an ethanol-ether-based solvent and base treated with monomethylamine as described (65). Lipids were desalted with butanol and analyzed by MS.

Lipid analyses

Lipids isolated from epidermal extracts were first analyzed by TLC. Lipids corresponding to 0.5 mg dry weight were spotted on HPTLC plates (Silicagel 60 F_{254}, Merck) using a Linomat IV (Camag). Afterwards, lipids were separated sequentially with the following solvent systems: (i) chloroform/acetone (1/1) for 4 cm, (ii) chloroform/methanol/glacial acetic acid (60/35/8) for 7 cm, (iii) chloroform/methanol/glacial acetic acid (190/9/1) for 12 cm, and (iv) n-hexane/methyl t-butyl ether/glacial acetic acid (90/10/1) until the top (20 cm). In between the different solvent systems, plates were thoroughly dried under vacuum. Bands were then made visible by spraying the TLC plates in 10% copper sulphate in 8% sulphuric acid and developing at 180°C.

Quantification of SLs was performed by tandem MS (triple quadrupole instrument equipped with a nano-electrospray source, VG micromass model Quattro II, Waters) according to reference (48). Equivalent lipid samples regarding the protein content were dissolved in 5 mM ammonium acetate in methanol. Prior to being analyzed, internal standards were added to the aliquots. Linoleic acid-esterified ωh-SLs were determined by subtraction of the amount of free ωh-SLs of the non-treated epidermal extracts from the respective amounts of ωh-SLs evaluated after saponification.

Epidermal sphingosine levels were quantified with a novel assay based on derivation of sphingosine prior to tandem MS (unpublished data).

For the quantification of yeast extracts, lipids were introduced into a Varian 320MS triple quadrupole in LC mode by direct infusion in methanol/chloroform/water (7/2/1, containing 2 mM ammonium acetate) (66). To quantify lipid species, multiple ion monitoring was used for each species (65). The recoveries and amounts of different IPC species were calculated relative to the GlcCer (d18:1, 8:0) standard according to a standard curve. Results are presented as a percentage of total IPCs detected because absolute amounts could not be determined without internal standards.

Epidermal protein isolation and western blotting

Skin samples were incubated at 58°C for 6 min in PBS containing 10 mM ethylenediaminetetraacetic acid (EDTA) in order to separate dermis from epidermis. Skin was then transferred into ice-cold PBS-EDTA solution and epidermis was obtained by peeling off the dermis. Epidermis in digitonin lysis buffer [20 mM HEPES-NaOH buffer (pH 7.4) containing 25 mM KCl, 250 mM sucrose, 2 mM $MgCl_2$, with freshly added 1% digitonin (Sigma), complete protease inhibitors (Roche) and 0.5 mM DTT] was homogenized by sonication (Branson sonifier 250) using five pulses every 30 s for 5 min. Lysates containing epidermal proteins were cleared by centrifugation at ∼21 000*g* for 15 min. Equal amounts of protein (50 μg) were separated by sodium dodecyl sulfate-polyacrylamide gel electrophoresis, blotted onto nitrocellulose membranes, incubated with primary antibodies overnight at 4°C and secondary antibody for 45–60 min at RT (details in Tables 4 and 5).

Light and electron microscopy

All morphological data included a minimum of two animals per group. Mouse embryos (E18.5) and newborns were anesthetized and transcardially perfused for 5–10 min with 3.5–4% glutaraldehyde in 0.1 M sodium cacodylate buffer (pH 7.6) containing saturated picric acid (300 μl per 100 ml fixative solution), 2% polyvinylpyrrolidone (PVP, Polyvidon 25, MW 25000, Merck) and 0.05% $CaCl_2$. Interscapular skin samples were removed and additionally postfixed overnight in the same fixative. In order to preserve the periderm and the adherent SC layers, samples were embedded in agar (Extrapure, Merck). Sections of 80–150 μm thickness were prepared using a microslicer (Dosaka DTK 1000). Sample processing followed three different procedures tested for optimal visualization of LB and ELL structure as well as keratinocyte morphology. Following the protocol of reference (67), the first series were treated with 0.25% RuO_4 (Polysciences) in 0.1 M sodium cacodylate buffer, pH 6.8 containing 0.5% potassium ferrocyanide for 15 min (Supplementary Material, Fig. S3A_1). The second series was postfixed according to reference (68) with 1% buffered OsO_4 in 0.1 M sodium cacodylate buffer, pH 7.6 for 90 min, followed by treatment with 1% tannic acid (Merck) in 0.5 M sodium cacodylate buffer, pH 7.5 for 10 min. Sections were immersed in the same buffer containing 1% Na_2SO_4 for 90 s (Supplementary Material, Fig. S3A_2). As described (69), the third series was incubated 60 min in alkaline DAB for selective catalase visualization and enhancement of membrane staining. Sections were postfixed with 1.5% buffered OsO_4 in sodium cacodylate buffer, pH 7.6 containing 1.5% potassium ferrocyanide for 20–30 min, followed then by osmification without ferrocyanide for an additional 40–60 min. En bloc staining was performed with 1% uranyl acetate for 20–30 min (Supplementary Material, Fig. S3A_3). Samples of all three series were washed with the respective buffers and processed for embedding in Epon 812.

Fixed on Superfrost® slides, serial semithin sections of 0.5–1 μm thickness were prepared (Leica Ultracut UCT) and stained with periodic acid-Schiff (PAS) as described (70). Briefly, Epon

Table 4. Primary antibodies used for immunofluorescence and immunoblots

Antibody	Gene name	Host/ligand—clonality[a]	Application[b]	Dilution	Supplier (clone)	Order num.
β-Actin	*Actb*	Rabbit—p	WB	1:1000	Santa Cruz	sc-1616-R
F-Actin	–	TRITC-phalloidin	Cryo SM	1:600	Sigma	P1951
Cathepsin D	*Ctsd*	Rabbit—p	WB	1:500	Dako	A0561
			Paraffin	1:100–200	Cytomation	
CerS3	*Cers3 (Lass3)*	Rabbit—p	Paraffin	1:1000	PickCell Laboratories	Custom-made[c]
Cholesterol	–	Filipin	Unfix. cryo	10 μg/ml	Sigma	F9765
Cingulin	*Cgn*	Guinea Pig—p	Unfix. cryo	1:2000	Provided by L. Langbein	–
Claudin1	*Cldn1*	Rabbit—p	WB	1:100	Thermo Scientific	RB-9209
			Unfix. cryo	1:10		
Dansyl[d]	–	Rabbit—p	Unfix. cryo	1:100	Invitrogen	A6398
Desmoglein 1/2	*Dsg1/2*	Mouse— m	WB	1:100	Provided by H. Heid (Progen, DG3.10)	61002
			Paraffin	1:10		
			Cryo SM	1:5		
Desmoplakin 1/2	*Dsp1/2*	Mouse—m	WB	1:50	Provided by H. Heid (Progen, DP447)	651155
			Paraffin	Undil.		
(Pro)Filaggrin	*Flg*	Rabbit—p	WB	1:1000	Covance	PRB-417P
			Paraffin	1:50		
GFP	*Gfp*	Rabbit—p	WB	1:1000	Genetex	GTX26556
Golgin-97 (Golgin A1)	*Golga1*	Mouse—m	ICC	1:200	Molecular Probes	A-21270
Involucrin	*Ivl*	Rabbit—p	WB	1:100	Thermo Scientific	RB-10288
			Cryo SM	1:150	Covance	PRB-140C
			Paraffin	1:100		
Kalilkrein 5	*Klk5*	Rabbit—p	WB	1:100	Abgent	AP6324b
Keratin 10	*Krt10*	Guinea Pig—p	Unfix. cryo	1:5000	Provided by L. Langbein	–
Keratin 14	*Krt14*	Guinea Pig—p	Unfix. cryo	1:3000	Provided by L. Langbein	–
Ki67	*MKi67*	Rat—m	Paraffin	1:200	Dako (TEC-3)	M7249
Lysosomal-associated membr. prot. 1	*Lamp1*	Rabbit—p	ICC	1:200	Acris	SP5446P
Loricrin	*Lor*	Rabbit—p	WB	1:1000	Covance	PRB-145P
			Cryo SM	1:150		
			Paraffin	1:100		
Polar and neutral lipids	–	Nile red	Unfix. cryo	5 μg/ml	MP Biomedicals	151744
Protein disulphide isomerase	*Pdi*	Mouse—m	ICC	1:400	Acris	SM5075
Peroxisomal biogenesis factor 14	*Pex14*	Rabbit—p	Unfix. cryo	1:100	Protein Tech Group	10594-1-AP
Plakoglobin	*Jup*	Mouse—m	WB	1:200	Provided by H. Heid (Progen, PG 5.1)	65105
Transgluta-minase 1	*Tgm1*	Rabbit—p	WB	1:4000	Abcam	ab86589

[a]m, monoclonal; p, polyclonal.
[b]Cryo SM: ultracryosemithin sections; ICC: immunocytochemistry of HeLa cells; Paraffin: paraffin sections; Unfix. cryo: unfixed cryo-sections; WB: western blot.
[c]Custom-made against a peptide located at the C-terminus of the mouse CerS3.
[d]Against monodansylcadaverine for *in situ* transglutaminase 1 assay.

Table 5. Secondary antibodies used for immunofluorescence and immunoblots

Antibody	Host/ligand	Application[a]	Dilution	Supplier	Order num.
Alexa Fluor® 546 anti-rabbit	Goat	ICC	1:400	Molecular Probes	A11035
Alexa Fluor® 488 anti-guinea pig	Goat	IHC	1:200	Molecular Probes	A11073
Biotinylated anti-rat	Rabbit	Paraffin	1:200	Vector Laboratories	BA-4001
Cy3™ anti-mouse	Donkey	ICC/IHC	1:200/1:1000	Jackson Dianova	715-165-150
Cy3™- anti-rabbit	Donkey	IHC	1:1000	Jackson Dianova	711-165-152
Mouse HRP	Goat	WB	1:1000	Santa Cruz	Sc-2005
Rabbit HRP	Goat	WB	1:1000	Santa Cruz	Sc-2004

[a]ICC, immunocytochemistry of HeLa cells; IHC, immunohistochemistry of tissue; WB, western blot.

sections were immersed in a freshly prepared 5% periodic acid solution at 60°C for 2 × 30 min, rinsed in distilled H_2O for 30 min and dried at 85°C. Sections were then incubated with Schiff solution for 90 min (2 × 45 min) at 60°C, with an additional rinsing and drying step. Subsequently, samples were counterstained with a modified Richardson solution containing

0.5% methylene blue/azure II (1:1) and 16% succrose in 0.5% aqueous borax solution for 1–3 min at RT. Specimens were finally rinsed with distilled H_2O and dried at 85°C. To visualize epidermal glycogen, specimens were exclusively stained with PAS without counterstaining.

For ultrastructural analysis, series of ultrathin Epon sections were stained with lead citrate prior to electron microscopical analysis (Zeiss EM 906E).

Light microscopical analysis of C. albicans *invasion*. Inoculated skin samples grown on collagen gels were fixed with 4% formalin for 24 h and subsequently embedded in paraffin. Sections (Microm, HM 355S) of 1 μm thickness were prepared, deparaffinized and stained with PAS: 0.75% periodic acid solution for 10 min, Schiff solution for 5 min. Following rinsing and drying steps, sections were counterstained with Mayer's hemalaun (Roth). Sections were dehydrated and mounted with Vitro-Clud (Langenbrink) and analyzed using a Leica DMLB microscope.

Immunohistochemistry

To guarantee optimal morphology, mice were transcardially perfused with 3–4% paraformaldehyde (PFA) in 0.1 M PBS, pH 7.4 containing 2% PVP for 5–10 min. Interscapular skin samples were postfixed for additional 30–60 min at 4°C and rinsed with PBS containing 2% PVP. These samples were used for paraffin sections and after embedding in agar for ultracryosemithin sections.

Paraffin sections. Specimens were dehydrated and embedded in Paraplast Plus. Sections of 3–5 μm thickness were obtained with a Microm HM 340E, then deparaffinized and subjected to antigen retrieval with 10 mM sodium citrate and 0.5% Tween-20 (pH 6.0) for 20 min at 96°C. Ctsd, desmoglein 1/2, desmoplakin 1/2, (pro)filaggrin, loricrin and CerS3 were detected according to this protocol.

In situ *mild alkaline hydrolysis*. For extraction of protein-bound SLs, paraffin sections were deparaffinized and immersed in 100% ethanol followed by 100% methanol. Mild alkaline methanolysis was performed (0.1 M KOH in 95% methanol) for 2 h at RT. Sections were carefully rinsed in methanol, immersed in 100% ethanol, dehydrated and rinsed in distilled water prior to antigen retrieval as described. Desmoglein 1/2, loricrin and involucrin were subjected to this protocol.

Ultracryosemithin sections. Microslicer sections of 600 μm thickness were cryoprotected in sucrose (10%, 20%, 30% and 2.3 M in 0.1 M PBS, pH 7.6 containing 10% PVP) prior to be frozen in isopentane precooled with liquid nitrogen. Subsequently, ultracryosemithin sections of 0.6–0.8 μm thickness were prepared with a Leica Ultracut UCT equipped with a Leica EMFCS and immunolabeled for F-actin, loricrin, desmoglein 1/2 and involucrin.

For the detection of sensitive antigens, unfixed interscapular skin samples were removed from anesthetized neonates and quickly placed onto a straight aluminum foil, immersed in OCT (Tissue Tek) and frozen in isopentane precooled with liquid nitrogen. Cryosections of 3–5 μm thickness were obtained with a Leica CM 3050S and subsequently fixed with acetone for 10 min at RT. For the detection of claudin 1, sections were subjected to an antigen retrieval as described. In order to localize cingulin and keratins 10 and 14, sections were permeabilized with 0.1% Triton X-100 in PBS (v/v) for 5 min and then blocked for 30 min with 10% fetal calf serum.

Transglutaminase 1 activity assay. Transglutaminase activity was localized as described with slight modifications (71). Shortly, unfixed fresh skin cryosections of 3–5 μm thickness were air-dried for 30 min and rinsed in PBS. Sections were blocked with 1% BSA in 100 mM Tris buffer (pH 7.4) for 30 min, following 1 h incubation with 12 μM monodansylcadaverine (Sigma) in 100 mM Tris buffer (pH 7.4) containing 5 mM calcium chloride. For negative controls, EDTA was added into the substrate buffer to a final concentration of 20 mM. The enzymatic reaction was stopped with 10 mM EDTA in PBS for 5 min. After rinsing in PBS, sections were incubated for 3 h with anti-dansyl in 12% BSA-PBS. Subsequently, sections were washed and incubated for 45 min with a secondary antibody in 12% BSA-PBS. Following nuclear staining, specimens were mounted and directly analyzed.

Immunolabeling. Ultracryosemithin-, cryo- and paraffin sections were incubated with primary antibodies for 1–16 h at 4°C or at RT (antibodies and the concentrations used are listed in Table 4). Incubation with secondary antibodies (see Table 5) was carried out for 1 h at RT.

For detection of nuclei and residual DNA, staining with DAPI (20 ng/ml, Sigma) or Draq5™ (Biostatus) was performed. Sections were mounted in either Fluoromount-G or DakoCytomation fluorescent mounting medium. For negative controls, PBS was used instead of primary antibodies. Sections were visualized with the fluorescence microscope Biorevo BZ-9000 (Keyence).

Proliferation assay with Ki67. Interfollicular keratinocyte proliferation was assessed in paraffin sections of PFA fixed skin using Ki67 as a marker (DakoAutostainer). Following binding with primary antibody, sections were incubated with a biotinylated anti-rat antibody and detected with alkaline phosphatase-labeled streptavidin (Tables 4 and 5).

Terminal dUTP nick-end labeling. TUNEL assay was performed on unfixed skin cryosections embedded in paraffin using the *in situ* cell death detection kit (Roche) and the recommendations provided by the manufacturer. After staining with Mayer's hemalaun, the sections were analyzed using a Leica DM-RBE microscope.

Localization of cholesterol and neutral lipids with filipin and Nile red

Unfixed cryosections were stained with filipin (cholesterol) or with Nile red (neutral lipids) as previously reported with slight modifications (72,73). Sections were air-dried, rinsed, fixed in 4% phosphate-buffered formalin and stained either with

freshly prepared filipin (10 μg/ml in PBS with 1% DMSO) for 2 h or with freshly prepared Nile red (5 μg/ml in 75% glycerol) for 5 min. Specimens were mounted in Fluoromount-G and analyzed (Biorevo BZ-9000, Keyence).

CerS3 localization in cultured HeLa cells

For subcellular localization of CerS3, HeLa cells were seeded and transfected with lipofectamine on sterile 12 mm glass cover slips. Following 24 h after transfection with mCerS3-EGFP plasmid, cells were washed with chilled PBS. CerS3 expressing cells were fixed with 3.5% PFA for 5 min on ice and for 10 min at RT. After permeabilization with methanol (−20°C, 6 min) (74), blocking was carried out for 1 h with 3% BSA-PBS. Primary antibodies were incubated for 1.5 h and secondary antibodies for 45 min at R. Immunofluorescence images were acquired with a Leica TCS-SL microscope using Leica Confocal software (version 2.61).

Generation and purification of CerS3 antibody

A synthetic peptide located at the C-terminus of mouse CerS3 protein was generated to immunize rabbits (PickCell Laboratories). The antiserum containing the polyclonal antibody was purified by affinity chromatography using the corresponding peptide coupled to *N*–hydroxysuccinimide-activated sepharose. The purified antibody was eluted with a low pH glycine buffer (70 mM glycine in 0.6 mM phosphate buffer pH 2.7) and concentrated using an Amicon Ultra 15 centrifugal filter device (Millipore) at 4000*g* for 20 min. Protein concentration was determined to 11.6 mg/ml.

Statistical analysis

Statistical analysis was performed using Student's *t*-test, and differences among groups were considered significant for $P < 0.05$ (*), $P < 0.01$ (**) and $P < 0.001$ (***).

SUPPLEMENTARY MATERIAL

Supplementary Material is available at *HMG* online.

ACKNOWLEDGEMENTS

The authors thank I. Kuhn-Krause, B. von Tümpling-Radosta, S. Kaden, C. Schmidt, T. Sijmonsma and R. Karayilan for excellent technical assistance, T. Miyazaki for sending genomic DNA of *Cers3* from a Japanese 129/Ola BAC library (75), Hexel and S. Schmitt for performing cell sorting, S. Wegehingel and H.-M. Müller for help in retroviral transduction, R. W. Owen for HPLC-purification of C28:0-CoA, I. Riezman for help with the Varian 320MS, B. Brügger for making the nanoESI-MS/MS available to us and H.-J. Stark, L. Langbein and H. Heid for kindly providing antibodies. We are very grateful to T. Klein for providing the fluorescence microscope Biorevo BZ-9000, Keyence.

Conflict of Interest statement. None declared.

FUNDING

This work was supported by the German Research Foundation (SA 1721/1-1 to R.S., SA 1721/2-1 to R.S., GO 432/2-1 to K.G. and SFB 645, B1 to K.W.); and by the Swiss National Science Foundation and the Swiss SystemsX.ch initiative, evaluated by the Swiss National Science Foundation to H.R.

REFERENCES

1. Madison, K.C. (2003) Barrier function of the skin: 'la raison d'etre' of the epidermis. *J. Invest. Dermatol.*, **121**, 231–241.
2. Elias, P.M., Williams, M.L., Holleran, W.M., Jiang, Y.J. and Schmuth, M. (2008) Pathogenesis of permeability barrier abnormalities in the ichthyoses: inherited disorders of lipid metabolism. *J. Lipid Res.*, **49**, 697–714.
3. Wertz, P.W. (1992) Epidermal lipids. *Semin. Dermatol.*, **11**, 106–113.
4. Arikawa, J., Ishibashi, M., Kawashima, M., Takagi, Y., Ichikawa, Y. and Imokawa, G. (2002) Decreased levels of sphingosine, a natural antimicrobial agent, may be associated with vulnerability of the stratum corneum from patients with atopic dermatitis to colonization by Staphylococcus aureus. *J. Invest. Dermatol.*, **119**, 433–439.
5. Nenoff, P. and Haustein, U.F. (2002) In vitro activity of phytosphingosines against Malassezia furfur and Candida albicans. *Acta Derm. Venereol.*, **82**, 170–173.
6. Payne, C.D., Ray, T.L. and Downing, D.T. (1996) Cholesterol sulfate protects Candida albicans from inhibition by sphingosine in vitro. *J. Invest. Dermatol.*, **106**, 549–552.
7. Veerman, E.C., Valentijn-Benz, M., van't Hof, W., Nazmi, K., van Marle, J. and Amerongen, A.V. (2010) Phytosphingosine kills Candida albicans by disrupting its cell membrane. *Biol. Chem.*, **391**, 65–71.
8. van Smeden, J., Hoppel, L., van der Heijden, R., Hankemeier, T., Vreeken, R.J. and Bouwstra, J.A. (2011) LC/MS analysis of stratum corneum lipids: ceramide profiling and discovery. *J. Lipid Res.*, **52**, 1211–1221.
9. Stiban, J., Tidhar, R. and Futerman, A.H. (2010) Ceramide synthases: roles in cell physiology and signaling. *Adv. Exp. Med. Biol.*, **688**, 60–71.
10. Lahiri, S. and Futerman, A.H. (2007) The metabolism and function of sphingolipids and glycosphingolipids. *Cell Mol. Life Sci.*, **64**, 2270–2284.
11. Laviad, E.L., Albee, L., Pankova-Kholmyansky, I., Epstein, S., Park, H., Merrill, A.H. Jr and Futerman, A.H. (2008) Characterization of ceramide synthase 2: tissue distribution, substrate specificity, and inhibition by sphingosine 1-phosphate. *J. Biol. Chem.*, **283**, 5677–5684.
12. Mizutani, Y., Mitsutake, S., Tsuji, K., Kihara, A. and Igarashi, Y. (2009) Ceramide biosynthesis in keratinocyte and its role in skin function. *Biochimie*, **91**, 784–790.
13. Rabionet, M., van der Spoel, A.C., Chuang, C.C., von Tumpling-Radosta, B., Litjens, M., Bouwmeester, D., Hellbusch, C.C., Korner, C., Wiegandt, H., Gorgas, K. *et al.* (2008) Male germ cells require polyenoic sphingolipids with complex glycosylation for completion of meiosis: a link to ceramide synthase-3. *J. Biol. Chem.*, **283**, 13357–13369.
14. Denic, V. and Weissman, J.S. (2007) A molecular caliper mechanism for determining very long-chain fatty acid length. *Cell*, **130**, 663–677.
15. Turgeon, B. and Meloche, S. (2009) Interpreting neonatal lethal phenotypes in mouse mutants: insights into gene function and human diseases. *Physiol. Rev.*, **89**, 1–26.
16. Hardman, M.J., Sisi, P., Banbury, D.N. and Byrne, C. (1998) Patterned acquisition of skin barrier function during development. *Development*, **125**, 1541–1552.
17. Elias, P.M., Feingold, K.R. and Fartasch, M. (2006) The Epidermal lamelar body as a multifunctional secretory organelle. In Elias, P.M. and Feingold, K.R. (eds), *Skin barrier*. Taylor & Francis Group, New York, USA, pp. 261–272.
18. Oren, A., Ganz, T., Liu, L. and Meerloo, T. (2003) In human epidermis, beta-defensin 2 is packaged in lamellar bodies. *Exp. Mol. Pathol.*, **74**, 180–182.
19. Ishida-Yamamoto, A., Simon, M., Kishibe, M., Miyauchi, Y., Takahashi, H., Yoshida, S., O'Brien, T.J., Serre, G. and Iizuka, H. (2004) Epidermal lamellar granules transport different cargoes as distinct aggregates. *J. Invest. Dermatol.*, **122**, 1137–1144.

20. Fransen, M., Terlecky, S.R. and Subramani, S. (1998) Identification of a human PTS1 receptor docking protein directly required for peroxisomal protein import. *Proc. Natl Acad. Sci. USA.*, **95**, 8087–8092.
21. Igarashi, S., Takizawa, T., Yasuda, Y., Uchiwa, H., Hayashi, S., Brysk, H., Robinson, J.M., Yamamoto, K., Brysk, M.M. and Horikoshi, T. (2004) Cathepsin D, but not cathepsin E, degrades desmosomes during epidermal desquamation. *Br. J. Dermatol.*, **151**, 355–361.
22. Fluhr, J. and Elias, P. (2002) Stratum corneum pH: Formation and function of the Acid Mantle. *Exog. Dermatol.*, **1**, 163–175.
23. Morita, K., Itoh, M., Saitou, M., Ando-Akatsuka, Y., Furuse, M., Yoneda, K., Imamura, S., Fujimoto, K. and Tsukita, S. (1998) Subcellular distribution of tight junction-associated proteins (occludin, ZO-1, ZO-2) in rodent skin. *J. Invest. Dermatol.*, **110**, 862–866.
24. Furuse, M., Hata, M., Furuse, K., Yoshida, Y., Haratake, A., Sugitani, Y., Noda, T., Kubo, A. and Tsukita, S. (2002) Claudin-based tight junctions are crucial for the mammalian epidermal barrier: a lesson from claudin-1-deficient mice. *J. Cell Biol.*, **156**, 1099–1111.
25. Sandilands, A., Sutherland, C., Irvine, A.D. and McLean, W.H. (2009) Filaggrin in the frontline: role in skin barrier function and disease. *J. Cell Sci.*, **122**, 1285–1294.
26. Kalinin, A.E., Kajava, A.V. and Steinert, P.M. (2002) Epithelial barrier function: assembly and structural features of the cornified cell envelope. *Bioessays*, **24**, 789–800.
27. Nemes, Z., Marekov, L.N., Fesus, L. and Steinert, P.M. (1999) A novel function for transglutaminase 1: attachment of long-chain omega-hydroxyceramides to involucrin by ester bond formation. *Proc. Natl Acad. Sci. USA*, **96**, 8402–8407.
28. Mizutani, Y., Kihara, A. and Igarashi, Y. (2006) LASS3 (longevity assurance homologue 3) is a mainly testis-specific (dihydro)ceramide synthase with relatively broad substrate specificity. *Biochem. J.*, **398**, 531–538.
29. Spassieva, S., Seo, J.G., Jiang, J.C., Bielawski, J., Alvarez-Vasquez, F., Jazwinski, S.M., Hannun, Y.A. and Obeid, L.M. (2006) Necessary role for the Lag1p motif in (dihydro)ceramide synthase activity. *J. Biol. Chem.*, **281**, 33931–33938.
30. Gimeno, R.E. (2007) Fatty acid transport proteins. *Curr. Opin. Lipidol.*, **18**, 271–276.
31. Sandhoff, R. (2010) Very long chain sphingolipids: tissue expression, function and synthesis. *FEBS Lett.*, **584**, 1907–1913.
32. Uchida, Y. and Holleran, W.M. (2008) Omega-O-acylceramide, a lipid essential for mammalian survival. *J. Dermatol. Sci.*, **51**, 77–87.
33. Akiyama, M. (2010) ABCA12 mutations and autosomal recessive congenital ichthyosis: a review of genotype/phenotype correlations and of pathogenetic concepts. *Hum. Mutat.*, **31**, 1090–1096.
34. Klar, J., Schweiger, M., Zimmerman, R., Zechner, R., Li, H., Torma, H., Vahlquist, A., Bouadjar, B., Dahl, N. and Fischer, J. (2009) Mutations in the fatty acid transport protein 4 gene cause the ichthyosis prematurity syndrome. *Am. J. Hum. Genet.*, **85**, 248–253.
35. Sidransky, E. (2004) Gaucher disease: complexity in a 'simple' disorder. *Mol. Genet. Metab.*, **83**, 6–15.
36. Uchida, Y., Cho, Y., Moradian, S., Kim, J., Nakajima, K., Crumrine, D., Park, K., Ujihara, M., Akiyama, M., Shimizu, H. *et al.* (2010) Neutral lipid storage leads to acylceramide deficiency, likely contributing to the pathogenesis of Dorfman-Chanarin syndrome. *J. Invest. Dermatol.*, **130**, 2497–2499.
37. Radner, F.P., Streith, I.E., Schoiswohl, G., Schweiger, M., Kumari, M., Eichmann, T.O., Rechberger, G., Koefeler, H.C., Eder, S., Schauer, S. *et al.* (2010) Growth retardation, impaired triacylglycerol catabolism, hepatic steatosis, and lethal skin barrier defect in mice lacking comparative gene identification-58 (CGI-58). *J. Biol. Chem.*, **285**, 7300–7311.
38. Vasireddy, V., Uchida, Y., Salem, N. Jr, Kim, S.Y., Mandal, M.N., Reddy, G.B., Bodepudi, R., Alderson, N.L., Brown, J.C., Hama, H. *et al.* (2007) Loss of functional ELOVL4 depletes very long-chain fatty acids (> or =C28) and the unique omega-O-acylceramides in skin leading to neonatal death. *Hum. Mol. Genet.*, **16**, 471–482.
39. Yanagi, T., Akiyama, M., Nishihara, H., Sakai, K., Nishie, W., Tanaka, S. and Shimizu, H. (2008) Harlequin ichthyosis model mouse reveals alveolar collapse and severe fetal skin barrier defects. *Hum. Mol. Genet.*, **17**, 3075–3083.
40. Vaglio, S. (2009) Chemical communication and mother-infant recognition. *Commun. Integr. Biol.*, **2**, 279–281.
41. Brouette-Lahlou, I., Godinot, F. and Vernet-Maury, E. (1999) The mother rat's vomeronasal organ is involved in detection of dodecyl propionate, the pup's preputial gland pheromone. *Physiol. Behav.*, **66**, 427–436.
42. Yamazaki, K., Beauchamp, G.K., Curran, M., Bard, J. and Boyse, E.A. (2000) Parent-progeny recognition as a function of MHC odortype identity. *Proc. Natl Acad. Sci. USA*, **97**, 10500–10502.
43. Macheleidt, O., Kaiser, H.W. and Sandhoff, K. (2002) Deficiency of epidermal protein-bound omega-hydroxyceramides in atopic dermatitis. *J. Invest. Dermatol.*, **119**, 166–173.
44. Ishikawa, J., Narita, H., Kondo, N., Hotta, M., Takagi, Y., Masukawa, Y., Kitahara, T., Takema, Y., Koyano, S., Yamazaki, S. *et al.* (2010) Changes in the ceramide profile of atopic dermatitis patients. *J. Invest. Dermatol.*, **130**, 2511–2514.
45. Paige, D.G., Morse-Fisher, N. and Harper, J.I. (1994) Quantification of stratum corneum ceramides and lipid envelope ceramides in the hereditary ichthyoses. *Br. J. Dermatol.*, **131**, 23–27.
46. Candi, E., Schmidt, R. and Melino, G. (2005) The cornified envelope: a model of cell death in the skin. *Nat. Rev. Mol. Cell Biol.*, **6**, 328–340.
47. Djian, P., Phillips, M., Easley, K., Huang, E., Simon, M., Rice, R.H. and Green, H. (1993) The involucrin genes of the mouse and the rat: study of their shared repeats. *Mol. Biol. Evol.*, **10**, 1136–1149.
48. Jennemann, R., Sandhoff, R., Langbein, L., Kaden, S., Rothermel, U., Gallala, H., Sandhoff, K., Wiegandt, H. and Grone, H.J. (2007) Integrity and barrier function of the epidermis critically depend on glucosylceramide synthesis. *J. Biol. Chem.*, **282**, 3083–3094.
49. Scharschmidt, T.C., Man, M.Q., Hatano, Y., Crumrine, D., Gunathilake, R., Sundberg, J.P., Silva, K.A., Mauro, T.M., Hupe, M., Cho, S. *et al.* (2009) Filaggrin deficiency confers a paracellular barrier abnormality that reduces inflammatory thresholds to irritants and haptens. *J. Allergy Clin. Immunol.*, **124**, 496–506, 506 e491–496.
50. Heikkinen, J.E., Jarvinen, M. and Jansen, C.R. (1975) Purification and biochemical characterization of rat skin cathepsin D. *J. Invest. Dermatol.*, **65**, 272–278.
51. Fluhr, J.W., Behne, M.J., Brown, B.E., Moskowitz, D.G., Selden, C., Mao-Qiang, M., Mauro, T.M., Elias, P.M. and Feingold, K.R. (2004) Stratum corneum acidification in neonatal skin: secretory phospholipase A2 and the sodium/hydrogen antiporter-1 acidify neonatal rat stratum corneum. *J. Invest. Dermatol.*, **122**, 320–329.
52. Jonca, N., Leclerc, E.A., Caubet, C., Simon, M., Guerrin, M. and Serre, G. (2011) Corneodesmosomes and corneodesmosin: from the stratum corneum cohesion to the pathophysiology of genodermatoses. *Eur. J. Dermatol.*, **21**, 35–42.
53. Zuo, Y., Zhuang, D.Z., Han, R., Isaac, G., Tobin, J.J., McKee, M., Welti, R., Brissette, J.L., Fitzgerald, M.L. and Freeman, M.W. (2008) ABCA12 maintains the epidermal lipid permeability barrier by facilitating formation of ceramide linoleic esters. *J. Biol. Chem.*, **283**, 36624–36635.
54. Li, W., Sandhoff, R., Kono, M., Zerfas, P., Hoffmann, V., Char-Hoa Ding, B., Proia, R.L. and Deng, C. (2007) Depletion of ceramides with very long chain fatty acids causes defective skin permeability barrier function, and neonatal lethality in ELOVL4 deficient mice. *Int. J. Biol. Sci.*, **3**, 120–128.
55. Oji, V., Tadini, G., Akiyama, M., Blanchet Bardon, C., Bodemer, C., Bourrat, E., Coudiere, P., DiGiovanna, J.J., Elias, P., Fischer, J. *et al.* (2010) Revised nomenclature and classification of inherited ichthyoses: results of the First Ichthyosis Consensus Conference in Soreze 2009. *J. Am. Acad. Dermatol.*, **63**, 607–641.
56. Puel, A., Cypowyj, S., Bustamante, J., Wright, J.F., Liu, L., Lim, H.K., Migaud, M., Israel, L., Chrabieh, M., Audry, M. *et al.* (2011) Chronic mucocutaneous candidiasis in humans with inborn errors of interleukin-17 immunity. *Science*, **332**, 65–68.
57. Dominguez-Villar, M. and Hafler, D.A. (2011) Immunology. An innate role for IL-17. *Science*, **332**, 47–48.
58. Puel, A., Picard, C., Cypowyj, S., Lilic, D., Abel, L. and Casanova, J.L. (2010) Inborn errors of mucocutaneous immunity to Candida albicans in humans: a role for IL-17 cytokines? *Curr. Opin. Immunol.*, **22**, 467–474.
59. Chamlin, S.L., Kao, J., Frieden, I.J., Sheu, M.Y., Fowler, A.J., Fluhr, J.W., Williams, M.L. and Elias, P.M. (2002) Ceramide-dominant barrier repair lipids alleviate childhood atopic dermatitis: changes in barrier function provide a sensitive indicator of disease activity. *J. Am. Acad. Dermatol.*, **47**, 198–208.
60. Engling, A., Backhaus, R., Stegmayer, C., Zehe, C., Seelenmeyer, C., Kehlenbach, A., Schwappach, B., Wegehingel, S. and Nickel, W. (2002) Biosynthetic FGF-2 is targeted to non-lipid raft microdomains following

translocation to the extracellular surface of CHO cells. *J. Cell Sci.*, **115**, 3619–3631.
61. Lucet-Levannier, K., Lellouche, J. and Mioskowski, C. (1995) Polysilylated coenzyme A for a high-yielding preparation of very lipophilic acyl coenzymes a in anhydrous organic sovents. *J. Am. Chem. Soc.*, **117**, 7546–7547.
62. Stark, H.J., Boehnke, K., Mirancea, N., Willhauck, M.J., Pavesio, A., Fusenig, N.E. and Boukamp, P. (2006) Epidermal homeostasis in long-term scaffold-enforced skin equivalents. *J. Investig. Dermatol. Symp. Proc.*, **11**, 93–105.
63. Germain, L., Rouabhia, M., Guignard, R., Carrier, L., Bouvard, V. and Auger, F.A. (1993) Improvement of human keratinocyte isolation and culture using thermolysin. *Burns*, **19**, 99–104.
64. Doering, T., Proia, R.L. and Sandhoff, K. (1999) Accumulation of protein-bound epidermal glucosylceramides in beta- glucocerebrosidase deficient type 2 Gaucher mice. *FEBS Lett.*, **447**, 167–170.
65. Guan, X.L., Riezman, I., Wenk, M.R. and Riezman, H. (2010) Yeast lipid analysis and quantification by mass spectrometry. *Methods Enzymol.*, **470**, 369–391.
66. Menuz, V., Howell, K.S., Gentina, S., Epstein, S., Riezman, I., Fornallaz-Mulhauser, M., Hengartner, M.O., Gomez, M., Riezman, H. and Martinou, J.C. (2009) Protection of C. elegans from anoxia by HYL-2 ceramide synthase. *Science*, **324**, 381–384.
67. Madison, K.C., Swartzendruber, D.C., Wertz, P.W. and Downing, D.T. (1987) Presence of intact intercellular lipid lamellae in the upper layers of the stratum corneum. *J. Invest. Dermatol.*, **88**, 714–718.
68. Simionescu, N. and Simionescu, M. (1976) Galloylglucoses of low molecular weight as mordant in electron microscopy. II. The moiety and functional groups possibly involved in the mordanting effect. *J. Cell. Biol.*, **70**, 622–633.
69. Komljenovic, D., Sandhoff, R., Teigler, A., Heid, H., Just, W.W. and Gorgas, K. (2009) Disruption of blood-testis barrier dynamics in ether-lipid-deficient mice. *Cell Tissue Res.*, **337**, 281–299.
70. Schroeder, H.E., Rossinsky, K. and Muller, W. (1980) An established routine method for differential staining of epoxy-embedded tissue sections. *Microsc. Acta*, **83**, 111–116.
71. Yanagi, T., Akiyama, M., Nishihara, H., Ishikawa, J., Sakai, K., Miyamura, Y., Naoe, A., Kitahara, T., Tanaka, S. and Shimizu, H. (2010) Self-improvement of keratinocyte differentiation defects during skin maturation in ABCA12-deficient harlequin ichthyosis model mice. *Am. J. Pathol.*, **177**, 106–118.
72. Goritz, C., Thiebaut, R., Tessier, L.H., Nieweg, K., Moehle, C., Buard, I., Dupont, J.L., Schurgers, L.J., Schmitz, G. and Pfrieger, F.W. (2007) Glia-induced neuronal differentiation by transcriptional regulation. *Glia*, **55**, 1108–1122.
73. Greenspan, P., Mayer, E.P. and Fowler, S.D. (1985) Nile red: a selective fluorescent stain for intracellular lipid droplets. *J. Cell Biol.*, **100**, 965–973.
74. Brock, R., Hamelers, I.H. and Jovin, T.M. (1999) Comparison of fixation protocols for adherent cultured cells applied to a GFP fusion protein of the epidermal growth factor receptor. *Cytometry*, **35**, 353–362.
75. Ohtsuka, M., Ishii, K., Kikuti, Y.Y., Warita, T., Suzuki, D., Sato, M., Kimura, M. and Inoko, H. (2006) Construction of mouse 129/Ola BAC library for targeting experiments using E14 embryonic stem cells. *Genes Genet. Syst.*, **81**, 143–146.
76. Dorschner, R.A., Lin, K.H., Murakami, M. and Gallo, R.L. (2003) Neonatal skin in mice and humans expresses increased levels of antimicrobial peptides: innate immunity during development of the adaptive response. *Pediatr. Res.*, **53**, 566–572.